




Star cluster progenitors are dynamically decoupled from their parent molecular clouds

Nicolas Peretto ¹★, Andrew J. Rigby ², Fabien Louvet,³ Gary A. Fuller,^{4,5} Alessio Traficante ⁶ and Mathilde Gaudel⁷

¹Cardiff Hub for Astrophysics Research & Technology, School of Physics & Astronomy, Cardiff University, Queens Buildings, The Parade, Cardiff CF24 3AA, UK

²School of Physics and Astronomy, University of Leeds, Leeds LS2 9JT, UK

³Université Grenoble Alpes, CNRS, IPAG, F-38000 Grenoble, France

⁴Jodrell Bank Center for Astrophysics, Department of Physics & Astronomy, University of Manchester, Oxford Road, Manchester M13 9PL, UK

⁵I. Physikalisches Institut, University of Cologne, Zùlpicher Str 77, D-50937 Köln, Germany

⁶IAPS-INAF, Via Fosso del Cavaliere, 100, I-00133 Rome, Italy

⁷LERMA, Observatoire de Paris, PSL Research University, CNRS, Sorbonne Université, F-75014 Paris, France

Accepted 2023 August 5. Received 2023 August 5; in original form 2023 March 17

ABSTRACT

The formation of stellar clusters dictates the pace at which galaxies evolve, and solving the question of their formation will undoubtedly lead to a better understanding of the Universe as a whole. While it is well known that star clusters form within parsec-scale overdensities of interstellar molecular gas called clumps, it is, however, unclear whether these clumps represent the high-density tip of a continuous gaseous flow that gradually leads towards the formation of stars, or a transition within the gas physical properties. Here, we present a unique analysis of a sample of 27 infrared dark clouds embedded within 24 individual molecular clouds that combine a large set of observations, allowing us to compute the mass and velocity dispersion profiles of each, from the scale of tens of parsecs down to the scale of tenths of a parsec. These profiles reveal that the vast majority of the clouds, if not all, are consistent with being self-gravitating on all scales, and that the clumps, on parsec-scale, are often dynamically decoupled from their surrounding molecular clouds, exhibiting steeper density profiles ($\rho \propto r^{-2}$) and flat velocity dispersion profiles ($\sigma \propto r^0$), clearly departing from Larson's relations. These findings suggest that the formation of star clusters correspond to a transition regime within the properties of the self-gravitating molecular gas. We propose that this transition regime is one that corresponds to the gravitational collapse of parsec-scale clumps within otherwise stable molecular clouds.

Key words: stars: formation – ISM: clouds – ISM: kinematics and dynamics.

1 INTRODUCTION

Only a few years after the first detection of interstellar carbon monoxide, Zuckerman & Evans (1974) showed that if all the gas within dense interstellar clouds were to be freely collapsing as a result of their self-gravity then the star formation rate in the Milky Way should be $\sim 300 M_{\odot} \text{ yr}^{-1}$, two orders of magnitude larger than what it actually is ($\sim 2 M_{\odot} \text{ yr}^{-1}$ – e.g. Robitaille & Whitney 2010). In other words, molecular clouds convert only ~ 1 per cent of their mass into stars every cloud free-fall time, making star formation a very inefficient process (e.g. Krumholz & Tan 2007). Despite five decades of star formation research, the physics behind this fundamental property of molecular clouds remain to be fully understood. Over the years, a number of competing theories have been developed to explain the low star formation efficiency of molecular clouds. The main differences between those models reside in both the fraction of the volume/mass of any molecular cloud that undergoes gravitational collapse, along with the dynamical state of the gas that does not. In

one family of models, supersonic turbulence is the one mechanism responsible for defining the mass reservoirs accessible to individual protostars and, as a result, for setting the stellar initial mass function (e.g. Padoan, Nordlund & Jones 1997; Krumholz & McKee 2005; Hennebelle & Chabrier 2008; Hopkins 2012; Padoan et al. 2020). In those models, the low star formation efficiency is explained by the fact that those mass reservoirs represent only a couple of per cents of the molecular gas mass, the rest of the gas is either unbound or in quasi-static equilibrium and therefore does not directly participate to star formation. On the other hand, other models predict that the hierarchical gravitational collapse of molecular clouds is what drive their evolution (e.g. Hartmann & Burkert 2007; Ballesteros-Paredes et al. 2011; Vázquez-Semadeni, González-Samaniego & Colín 2017; Vázquez-Semadeni et al. 2019) and that massive star formation benefits from the favourable conditions generated by the global collapse of dense clumps (e.g. Bonnell & Bate 2006; Peretto, Hennebelle & André 2007; Smith, Longmore & Bonnell 2009). In those models, what limits the efficiency of star formation is stellar feedback from young low- and high-mass stars, by stabilizing or dispersing most of the molecular cloud's mass (e.g. Nakamura & Li 2007; Wang et al. 2010; Dale, Ercolano & Bonnell 2012; Kim,

* E-mail: nicolas.peretto@astro.cf.ac.uk

Kim & Ostriker 2018; Offner & Liu 2018; Grudić et al. 2022). The controversy around which of these two very different scenarios of star formation describes reality best fuels the majority of the star formation research for the past 20 yr or so.

A large number of studies have looked at the gravitational binding of molecular clouds and their substructures within, most often via the calculation of their virial parameters (e.g. Larson 1981; Solomon et al. 1987; Heyer et al. 2009; Roman-Duval et al. 2010; Kauffmann, Pillai & Goldsmith 2013; Miville-Deschênes, Murray & Lee 2017; Schuller et al. 2017; Rigby et al. 2019; Duarte-Cabral et al. 2021). Depending on the cloud sample that is being studied, the methods that are being used, and the interpretation of the data that is being made, the conclusions range from molecular clouds are: in hydrostatic equilibrium, collapsing, or unbound. As a result, a consensus as yet to be found.

A possibly more insightful analysis of molecular clouds is the study of their internal virial ratio profiles. Indeed, if there is a scale/density threshold at which the gravitational binding of clouds change from unbound to bound as a result of, for instance, stellar feedback, then the virial ratio profiles of individual clouds should exhibit some breaks at that particular scale. While several studies have investigated the shape of the mass profiles of cores, clumps, and clouds (e.g. Motte & André 2001; Kauffmann et al. 2010; Palau et al. 2014; Barnes et al. 2021), studies that have looked into their virial ratio profiles are a lot more rare. This is the consequence of the much larger range of spatial scales probed by dust observations, most often used for structure mass estimates, compared to spectral line ones, needed to derive velocity dispersions of those structures. The few observational studies that have looked into the question of clouds' virial ratio radial profiles have done so either on single clouds (e.g. Rosolowsky et al. 2008; Goodman et al. 2009), using single tracers (e.g. Heyer et al. 2009; Li et al. 2015; Wong et al. 2019), or using only two radial points (e.g. Heyer et al. 2009; Traficante et al. 2018, 2020). As a result, the virial ratio radial profiles of molecular clouds have not been fully characterized yet. In this paper, we use a multiscale and multitracer approach that allows us to construct, in a uniform way, the virial ratio profiles of a sample of molecular clouds from scales of tenths of a parsec up to scales of tens of parsecs. In Section 2, we present the source selection and observations. Section 3 explains how the profiles of individual cloud are built. Section 4 presents the models we use to determine the origin of the observed profile features. In Section 5, we discuss our results while conclusions are laid out in Section 6.

2 SOURCE SELECTION AND OBSERVATIONS

2.1 Sample

We selected a sample of 27 infrared dark clouds (IRDCs) from the Spitzer Dark Cloud catalogue of Peretto & Fuller (2009). Compared to other cloud samples, IRDCs have the advantage that their heliocentric distances are better constrained, with a large majority of IRDCs lying at the near kinematic distance solution provided by Galactic rotation models (Ellsworth-Bowers et al. 2013). In this paper, the adopted distances for all IRDCs are the near kinematic distance solutions from the Reid et al. (2009) model. The selection criteria for these IRDCs are (a) the kinematic distance as estimated from $^{13}\text{CO}(1-0)$ GRS data (Roman-Duval et al. 2010) should be $d = 4(\pm 1)$ kpc; (b) selected IRDCs should exhibit a range of aspect ratios, i.e. from circular to filamentary, as measured from *Herschel* column density images (Peretto et al. 2016); (c) selected IRDCs should exhibit a range of mass and size as estimated from *Herschel*

column density images; (d) all IRDCs have to lie beyond $l = 15^\circ$ in order to be easily observed from the IRAM 30 m telescope. Global properties of the 27 selected clouds can be found in Table 1. Note that kinematic distances have been recalculated using the dense gas data presented in this paper, leading in a few cases to a departure from condition (a). Fig. 1(a) shows one of the selected IRDCs, images of the remaining 26 can be seen in Appendix A, which is supplied as online supplementary material.

2.2 Observations

In this study, we exploit four different data sets, each of which is tracing a specific density regime of molecular clouds and/or giving us access to different sets of information (mass versus kinematics). In the following, we describe each of these data sets.

2.2.1 $\text{N}_2\text{H}^+(1-0)$ data

We observed the 27 IRDCs at the IRAM 30 m between 2013 June 18 and 24, reaching a total of 42 h of telescope time. The weather conditions were stable with an average sky opacity at 230 GHz of 0.2. We mapped each region using the 90 Hz EMIR receiver in conjunction with the FTS spectrometer at 50 kHz spectral resolution, providing a velocity resolution of 0.16 km s^{-1} . Primary pointing and focus were performed on Saturn. The pointing accuracy was < 5 arcsec. In this study, we focus on the $\text{N}_2\text{H}^+(1-0)$ line, with an angular resolution of 28 arcsec. All data have been reduced using the CLASS package, and gridded into 9 arcsec pixel-size cubes. The final noise range from 0.09 to 0.2 K per velocity channel and pixel.

2.2.2 *Herschel* data

We used the PACS (Poglitsch et al. 2010) and SPIRE (Griffin et al. 2010) *Herschel* (Pilbratt et al. 2010) data from the Hi-GAL survey (Molinari et al. 2010). The Hi-GAL data were reduced, as described in Traficante et al. (2011), using HIPE (Ott 2010) for calibration and deglitching (SPIRE only), routines especially developed for Hi-GAL data reduction (drift removal, deglitching), and the ROMAGAL map-making algorithm. Post-processing on the maps was applied to help with image artefact removal (Piazzo et al. 2015). In this paper, we make use of the PACS 160 μm and SPIRE 250/450/500 μm data with a nominal angular resolution of 12, 18, 25, and 36 arcsec, respectively. In addition, zero-flux levels for every Hi-GAL field have been recovered by correlating *Herschel* data with Planck and IRAS data (Bernard et al. 2010).

2.2.3 $^{13}\text{CO}(1-0)$ and $^{12}\text{CO}(1-0)$ data

We used the FCRAO $^{13}\text{CO}(1-0)$ data from the Galactic Ring Survey (GRS; Jackson et al. 2006) along with the FCRAO UMSB $^{12}\text{CO}(1-0)$ data (Clemens et al. 1986; Sanders et al. 1986). The GRS data has an angular resolution of 44 arcsec, a velocity resolution of 0.21 km s^{-1} and a one σ noise of 0.13 K (in T_A^* scale). The main beam efficiency of the FCRAO telescope at the $^{13}\text{CO}(1-0)$ frequency is 0.48. All clouds from our sample of 27 IRDCs are covered by the GRS.

The UMSB $^{12}\text{CO}(1-0)$ data has a nominal angular resolution of 44 arcsec. However, the data have been sampled on a 3 arcmin grid, which effectively decreases the resolution. The velocity resolution is 1 km s^{-1} , and the one σ noise is 0.4 K (in T_R^* scale). In order to be able to convert that into a main beam temperature one needs first to multiply by $n_{\text{fbs}} = 0.7$ which converts the unit back to T_A^* (Kutner & Ulich 1981; Sanders et al. 1986) and then divide by the main beam

Table 1. IRDC sample.

Cloud ID	Name	Coordinates (J2000)	Systemic velocity (km s ⁻¹)	Distance (kpc)
1	SDC18.624−0.070	18:25:10.0 −12:43:45	+45.6	3.50
2	SDC18.787−0.286	18:26:19.0 −12:41:16	+65.4	4.36
3	SDC18.888−0.476	18:27:09.7 −12:41:32	+66.3	4.38
4	SDC21.321−0.139	18:30:32.1 −10:22:50	+66.5	4.24
5	SDC22.373+0.446	18:30:24.5 −09:10:34	+53.0	3.61
6	SDC22.724−0.269	18:33:38.3 −09:11:55	+73.3 (+105.0)	4.44
7	SDC23.066+0.049	18:33:08.2 −08:44:53	+91.8	5.11
8	SDC23.367−0.288	18:34:53.8 −08:38:00	+78.3 (+103.0; +58)	4.60
9	SDC24.118−0.175	18:35:52.6 −07:55:06	+80.9	4.68
10	SDC24.433−0.231	18:36:41.0 −07:39:20	+58.4	3.75
11	SDC24.489−0.689	18:38:25.7 −07:49:36	+48.1	3.28
12	SDC24.618−0.323	18:37:22.4 −07:32:18	+43.4	3.04
13	SDC24.630+0.151	18:35:38.2 −07:18:35	+53.2 (+115.0)	3.51
14	SDC25.166−0.306	18:38:13.0 −07:03:00	+63.6	3.95
15	SDC25.243−0.447	18:38:57.1 −07:02:20	+59.1	3.75
16	SDC26.507+0.716	18:37:07.9 −05:23:58	+48.3	3.21
17	SDC28.275−0.163	18:43:30.3 −04:12:45	+80.3	4.60
18	SDC28.333+0.063	18:42:54.1 −04:02:30	+79.3	4.56
19	SDC31.039+0.241	18:47:03.3 −01:33:50	+78.2 (+98; +110)	4.54
20	SDC34.370+0.203	18:53:18.9 +01:24:54	+57.9	3.59
21	SDC35.429+0.138	18:55:30.4 +02:17:10	+77.0	4.67
22	SDC35.527−0.269	18:57:08.6 +02:09:08	+45.4	2.95
23	SDC35.745+0.147	18:56:02.6 +02:34:44	+83.4	5.11
24	SDC38.850−0.427	19:03:46.8 +05:04:03	+42.2	2.81
25	SDC40.283−0.216	19:05:41.2 +06:26:09	+72.7	4.89
26	SDC47.061+0.257	19:16:41.8 +12:39:39	+57.0	4.64
27	SDC52.723+0.045	19:28:34.4 +17:34:17	+44.1	4.49

Note. Column 1: IRDC identification number; Column 2: IRDC name from Peretto & Fuller (2009); Column 3: Central IRDC coordinates; Column 4: Systemic LSR velocity of the clump as estimated from N₂H⁺(1–0), the velocities in between brackets correspond to the additional components identified in the spectra; Column 5: Near kinematic distance as estimated from the Reid et al. (2009) model, uncertainties on those are typically of the order of 10–20 per cent.

efficiency 0.48, so effectively multiplying the UMSB data set by a (0.7/0.48) factor.

3 MASS AND VELOCITY DISPERSION PROFILES

The goal of this paper is to determine how the ratio of kinetic to gravitational energy of clouds changes as a function of spatial scale. In order to observationally measure such ratio, one needs to determine three quantities: radius, mass, and velocity dispersion. While the cloud mass can reliably be determined via dust emission observations, no single molecular line can trace molecular gas velocity dispersion on all scales, either because of high optical depth or low abundance. We therefore need a combination of tracers to trace different parts of the cloud. Here, we use ¹³CO(1–0) to trace the large scales, more diffuse parts of the clouds, and N₂H⁺(1–0) to trace their densest parts. Fig. 2 shows a simple sketch that illustrates what tracer we use for what purpose. In the following subsections, we describe how we computed the three required quantities for both the dense and diffuse regions of the clouds.

3.1 Dense gas

3.1.1 Herschel column density maps of IRDCs

For the purpose of this study, we computed H₂ column density maps using the method presented in Peretto et al. (2016, referred to as P16 hereafter). That method consists in using the ratio of the *Herschel* 160 μm over 250 μm dust emission to measure the temperature of

the dust, and then use it, in combination with the 250 μm image to derive the column density of gas (assuming a dust to gas mass ratio of 1 per cent) at an angular resolution of 18 arcsec. For the purpose of the study presented here, we convolved the column density image to the same angular resolution as the N₂H⁺(1–0) data, i.e. 28 arcsec. The assumed specific dust opacity is $\kappa_{\lambda} = 0.1 \left(\frac{\lambda}{300 \mu\text{m}}\right)^{\beta} \text{cm}^2 \text{g}^{-1}$ (Hildebrand 1983), with $\beta = 1.8$ (e.g. Planck Collaboration XXV 2011; Sadavoy et al. 2016; Rigby et al. 2018).

When computing these maps, we make the assumption of a uniform temperature along the line of sight. This is of course incorrect but it is not completely clear though how wrong this assumption is for the structures we are studying. Since we might expect this assumption of a single temperature to be the most inaccurate towards the centre of each clump, we decided to compare the mass profiles of each clumps obtained with P16’s method with that of PPMAP (Marsh, Whitworth & Lomax 2015), a bayesian code that derive, from *Herschel* observations, the distribution of dust temperatures along the line of sight. Note that we do not use PPMAP in this paper as it can generate a number of artefacts around bright protostellar sources, it is computationally expensive, and arising issues are a lot less straightforward to identify than when using the P16’s method.

On the *y*-axis of Fig. 3 we show the ratio of the PPMAP over the P16 masses, radially averaged. On the *x*-axis of the same figure, we show the radial dispersion of that same ratio, i.e. how much it varies about the average value as a function of radius (i.e. 0 per cent means that the ratio is radially uniform). One can see that while, on average, the PPMAP masses are about 20 per cent larger than the P16 masses, the variations of the mass ratio as a function of radius are small, and remain below 5 per cent for most clouds, with a maximum standard

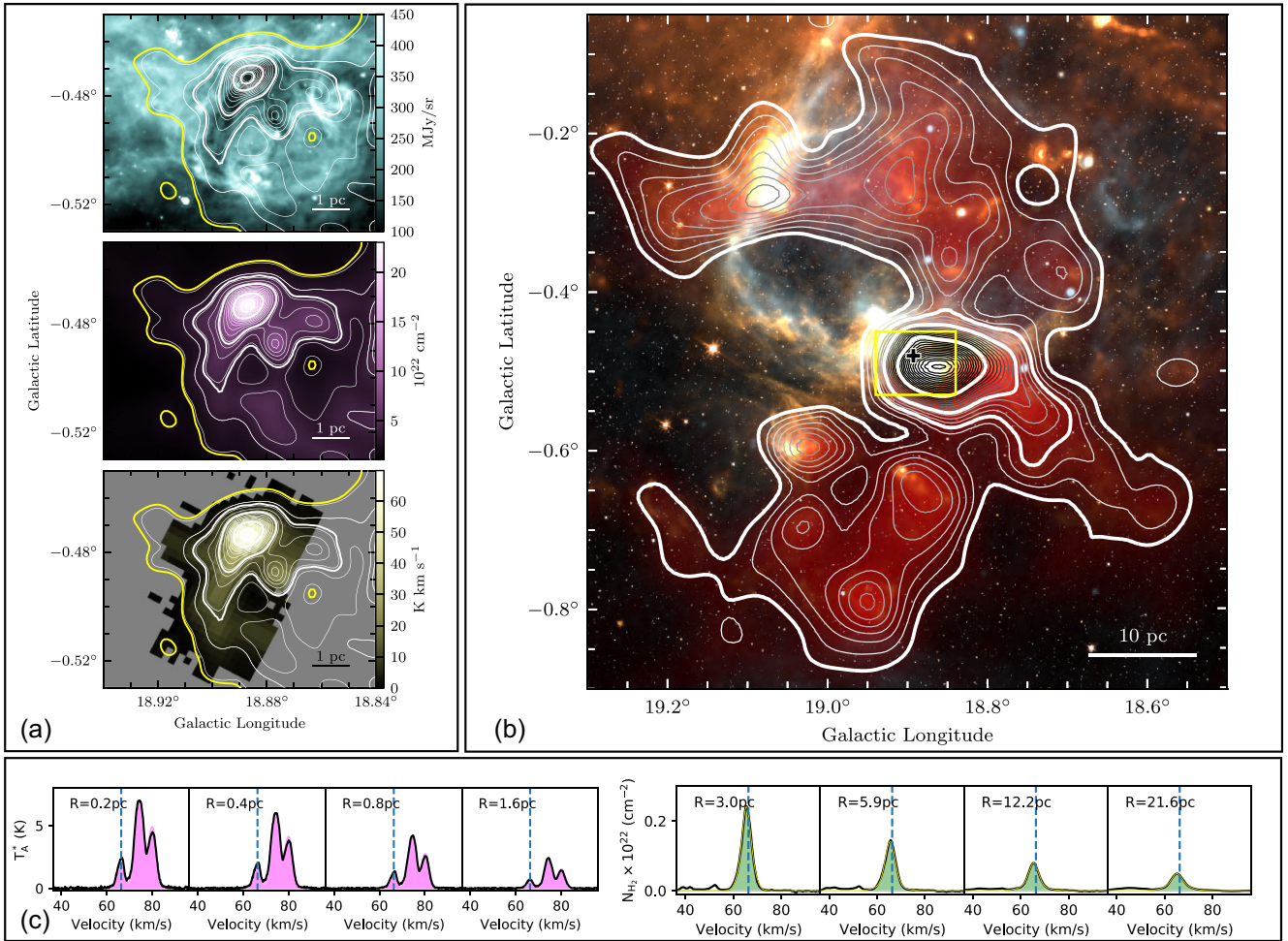


Figure 1. Images of SDC18.888-0.476. (a) Top – *Spitzer* 8 μm ; middle – H_2 column density from *Herschel* observations; bottom – $\text{N}_2\text{H}^+(1-0)$ integrated emission. The contours are identical in all panels, and are those of the H_2 column density image. The yellow contour corresponds to $N_{\text{N}_2\text{H}^+}^{\text{edge}}$. The four thicker white contours are those used to compute the average $\text{N}_2\text{H}^+(1-0)$ spectra displayed in magenta in panel (c), the first one of which corresponds to $N_{\text{N}_2\text{H}^+}^{\text{start}}$. (b) Multicolour image of the molecular cloud hosting the SDC18.888-0.476 infrared dark clump (white: 3.6 μm , orange: 8 μm , yellow: 70 μm , orange: 350 μm , blue: 1.42 GHz, red: H_2 column density). The contours show the H_2 column density obtained from the Galactic Ring Survey $^{13}\text{CO}(1-0)$ data. The thicker white contours are those used to compute the $^{13}\text{CO}(1-0)$ -based spectra shown in green in panel (c). The plus symbol shows the central position of the IRDC, and the yellow rectangle shows the coverage of the images displayed in (a). (c) Spectra averaged within the highlighted H_2 column density contours in panels (a) and (b). The radius of the region within which the spectra have been averaged are indicated in each panel. The vertical blue dashed lines show the systematic clump velocity as measured from $\text{N}_2\text{H}^+(1-0)$. The compilation of the data presented in this figure summarizes all the information used for each cloud in the study presented here. A similar figure for each remaining IRDC can be found in Appendix A.

deviation of less than 8 per cent. This shows that, while there might be a systematic uncertainty on the mass of 20 per cent, the shape of the mass profiles derived from both methods are very much consistent with each other.

3.1.2 $\text{N}_2\text{H}^+(1-0)$ as a tracer of *Herschel* clumps

All 27 IRDCs are detected in $\text{N}_2\text{H}^+(1-0)$. For 4 of them (~ 15 per cent), multiple clouds with velocities differing by more than 20 km s^{-1} have been identified within the observed field of views. For one of this IRDC (SDC31.039+0.241), the $\text{N}_2\text{H}^+(1-0)$ emission of the different clouds spatially overlap. This cloud is therefore excluded from the rest of the analysis as the origin of the corresponding dust continuum emission becomes very uncertain. Regarding the remaining three clouds (SDC22.724–0.269, SDC23.367–0.288, SDC24.630+0.151), we only consider the cloud for which the

$\text{N}_2\text{H}^+(1-0)$ integrated emission best matches the extinction feature seen in the mid-infrared. The corresponding velocities are provided in Table 1.

Another four IRDCs (SDC24.433–0.231, SDC24.630+0.151, SDC26.507+0.716, and SDC35.527–0.269) show multiple velocity components with velocity differences lower than 3 km s^{-1} , only one of these also exhibits multiple clouds along the line of sight (SDC24.630+0.151). However, once averaged within column density contours (see Appendix A), the multiple velocity components are mostly washed out, and are therefore not a concern in the context of this study. Note that one of the multiple velocity component cloud, i.e. SDC35.527–0.269, has been extensively studied in the past at high angular resolution clearly revealing multiple velocity component structures (e.g. Henshaw et al. 2014).

The morphology of the $\text{N}_2\text{H}^+(1-0)$ integrated intensity images are very similar to that of the H_2 *Herschel* column density maps (see

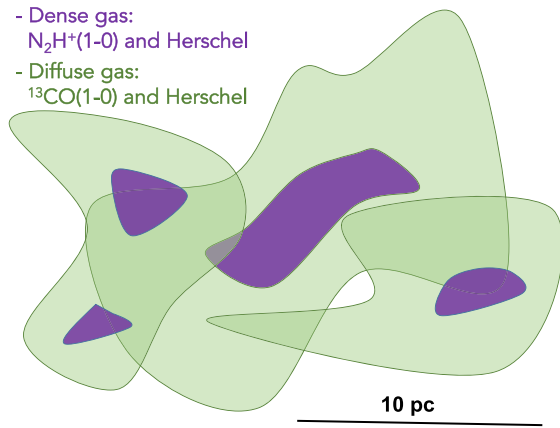


Figure 2. Sketch of molecular cloud configuration and relevant tracers. Diffuse gas (represented in green) is traced by $^{13}\text{CO}(1-0)$ and dust continuum. However, only the former is able to disentangle the emission of multiple clouds along the line of sight by segmenting them in velocity space. In this paper, we will use both tracers to constrain the mass and morphology of the clouds on the largest scales. Dense gas (represented in purple) is well probed by both dust continuum and molecular line tracers such as $\text{N}_2\text{H}^+(1-0)$. It is very rare that two $\text{N}_2\text{H}^+(1-0)$ cloud overlap (as the low frequency of multiple $\text{N}_2\text{H}^+(1-0)$ velocity components is showing). Dust continuum can therefore also be used once a background contamination (from the diffuse gas) has been removed.

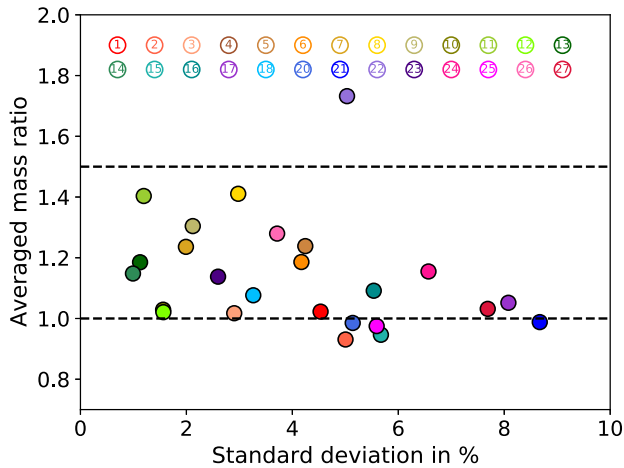


Figure 3. Ratio of the PPMAP masses over the P16 masses averaged over their radial profiles as a function of their mass ratio standard deviation. The black dashed lines show mass ratios of 1 and 1.5. Each colour corresponds to a single IRDC whose ID number can be found at the top of the figure (see Table 1 for the corresponding IRDC name). Note that IRDC SDC31.039+0.241 (ID number 19) has been left out as a result of the presence of multiple dense clumps present along the line of sight (see Section 3.1.2).

Fig. 1), qualitatively showing that $\text{N}_2\text{H}^+(1-0)$ is a good tracer of the column density structure of star-forming clouds. In order to quantify the correlation between dust column density and $\text{N}_2\text{H}^+(1-0)$ line emission we produced scatter plots for each cloud of the H_2 column density derived from *Herschel*, for which the background as defined by $N_{\text{N}_2\text{H}^+}^{\text{edge}}$ (see the next section) has been subtracted, versus the integrated intensity of $\text{N}_2\text{H}^+(1-0)$ (see Fig. 4 for four representative examples). One can see there is, indeed, a strong linear correlation between the two quantities, with only small departures from it for

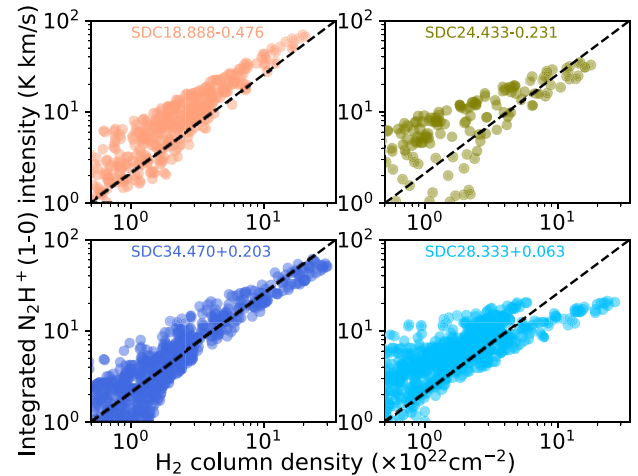


Figure 4. Scatter plots of the background subtracted H_2 column density versus the $\text{N}_2\text{H}^+(1-0)$ integrated intensity (in T_a^* scale) for four clumps. In each panel, the same linear relation is displayed as a dashed black line.

some clouds exhibiting a large range of different physical conditions (see the case of SDC28.333+0.063 in Fig. 4). We observe similar correlations for all clouds for which there is enough dynamic range and independent points (i.e. 21/27 clouds). We have also checked whether the relation provided by Hacar et al. (2018) between H_2 column density, $\text{N}_2\text{H}^+(1-0)$ integrated intensities, and temperature hold for our cloud sample. We can confirm that it does for most of the clumps, but some significant departures are observed, which can be explained by a variation of the N_2H^+ abundance by a factor of 2 or so. Nevertheless, from this comparison we can conclude that N_2H^+ is a good tracer of the dense gas as traced with *Herschel*, and therefore that we can reasonably use it to trace the kinematics of *Herschel* clumps for the (column) density range we are probing (i.e. $N_{\text{H}_2} \geq 10^{22} \text{ cm}^{-2}$). As such we do not expect the effect of using different tracers for mass and kinematics to be a significant issue in our study (see Traficante et al. 2018; Yuan, Krumholz & Burkhardt 2020).

3.1.3 Mass and velocity dispersion estimates

The resulting H_2 column density maps (see Fig. 1) are contaminated by foreground and background interstellar structures that are not physically associated with the cloud. Removing such contributions is not an easy task (Peretto et al. 2010; Battersby et al. 2011). In the context of this study, we are mostly interested in the part of the cloud which is seen in $\text{N}_2\text{H}^+(1-0)$ in the IRAM 30 m data. Therefore, we define the ‘edge’ of the dense part of the clouds as being the column density contour, $N_{\text{N}_2\text{H}^+}^{\text{edge}}$, that best matches the extent of the $\text{N}_2\text{H}^+(1-0)$ integrated intensity map. This is done by computing the median (along with the 16th and 84th percentiles) column density value within a ring just outside the $\text{N}_2\text{H}^+(1-0)$ integrated intensity contour of 0.5 K km s^{-1} , i.e. our detection limit. The value of $N_{\text{N}_2\text{H}^+}^{\text{edge}}$ will then serve as the background column density of the clump that we will remove from any clump scale mass measurements (see Table 2 for the individual values of $N_{\text{N}_2\text{H}^+}^{\text{edge}}$ and corresponding 16th and 84th percentiles).

We used the contour-based dendrogram tool from Peretto & Fuller (2009) on the *Herschel* column density maps to estimate sizes and masses of connected groups of pixels lying above a certain column density. In order to be considered for the analysis those groups of

Table 2. IRDCs and parent cloud properties.

ID	$N_{\text{N}_2\text{H}^+}^{\text{edge}}$ ($\times 10^{22}$ cm $^{-2}$)	$N_{\text{N}_2\text{H}^+}^{\text{start}}$ ($\times 10^{22}$ cm $^{-2}$)	$R_{\text{N}_2\text{H}^+}^{\text{start}}$ (pc)	$M_{\text{N}_2\text{H}^+}^{\text{start}}$ (M_{\odot})	$\sigma_{\text{N}_2\text{H}^+}^{\text{start}}$ (km s $^{-1}$)	$\alpha_{\text{vir}}^{\text{N}_2\text{H}^+}$	$R_{\text{CO}}^{\text{start}}$ (pc)	$M_{\text{CO}}^{\text{start}}$ ($\times 10^4 M_{\odot}$)	$\sigma_{\text{CO}}^{\text{start}}$ (km s $^{-1}$)	$\alpha_{\text{vir}}^{13\text{CO}}$
1	2.8 $^{+0.3}_{-0.2}$	3.3	1.66	3239 $^{+365}_{-546}$	0.99	0.62	12.62	14.52	5.74	3.35
2	2.4 $^{+0.4}_{-0.4}$	3.3	1.18	1807 $^{+365}_{-365}$	1.06	0.89	21.54	48.36	4.19	0.91
3	1.9 $^{+0.3}_{-0.3}$	3.7	1.61	7882 $^{+513}_{-513}$	1.55	0.58	21.63	47.30	3.72	0.74
4	3.2 $^{+0.3}_{-0.5}$	3.3	1.09	562 $^{+395}_{-237}$	0.69	1.20	9.02	3.71	2.81	2.25
5	2.3 $^{+0.4}_{-0.5}$	2.9	0.63	437 $^{+101}_{-81}$	1.13	2.03	3.46	0.31	1.39	2.61
6	3.3 $^{+0.7}_{-0.5}$	4.6	0.60	533 $^{+118}_{-164}$	0.65	0.62	11.58	11.85	4.50	2.32
7	3.2 $^{+0.4}_{-0.3}$	3.6	1.48	1536 $^{+434}_{-579}$	0.98	1.14	16.27	30.40	5.90	2.18
8	4.2 $^{+0.5}_{-0.5}$	6.1	0.72	1575 $^{+172}_{-172}$	1.17	0.76	17.76	27.61	3.67	1.02
9	2.6 $^{+0.3}_{-0.4}$	2.9	1.32	1318 $^{+462}_{-346}$	1.03	1.31	6.46	2.02	1.63	1.00
10	2.9 $^{+0.5}_{-0.5}$	3.1	1.39	3282 $^{+642}_{-642}$	1.50	1.14	5.23	2.31	2.88	2.21
11	1.2 $^{+0.2}_{-0.2}$	1.4	1.12	831 $^{+167}_{-167}$	1.13	2.08	9.19	2.18	1.67	1.39
12	2.0 $^{+0.3}_{-0.1}$	2.5	0.82	594 $^{+45}_{-134}$	0.85	1.26	12.67	5.85	1.63	0.68
13	2.7 $^{+0.5}_{-0.3}$	4.4	0.48	472 $^{+45}_{-75}$	1.08	1.42	6.80	3.34	3.58	3.06
14	2.2 $^{+0.2}_{-0.2}$	2.5	1.68	3622 $^{+374}_{-374}$	0.96	0.53	8.65	3.23	1.78	1.00
15	1.8 $^{+0.2}_{-0.2}$	2.0	1.33	1233 $^{+235}_{-235}$	0.84	0.95	13.11	13.35	4.23	2.05
16	1.7 $^{+0.3}_{-0.3}$	1.8	1.62	1474 $^{+518}_{-518}$	1.02	1.40	7.28	3.20	1.44	0.56
17	3.0 $^{+0.5}_{-0.3}$	3.7	1.53	2687 $^{+465}_{-775}$	1.27	1.10	31.13	98.02	4.31	0.69
18	4.4 $^{+0.4}_{-0.4}$	5.1	2.65	13954 $^{+1863}_{-1863}$	1.42	0.46	30.85	103.70	5.27	0.97
20	2.7 $^{+0.5}_{-0.4}$	3.5	2.15	12048 $^{+1223}_{-1528}$	1.34	0.39	11.33	18.13	3.79	1.05
21	2.7 $^{+0.4}_{-0.3}$	3.0	2.62	7761 $^{+1366}_{-2276}$	1.33	0.72	11.24	4.01	3.20	3.37
22	2.2 $^{+0.3}_{-0.2}$	2.7	1.36	1499 $^{+245}_{-367}$	0.77	0.68	8.22	3.49	1.89	0.99
23	1.9 $^{+0.1}_{-0.2}$	2.0	2.01	3490 $^{+536}_{-268}$	1.07	0.80	11.58	7.66	3.74	2.47
24	2.7 $^{+0.2}_{-0.2}$	2.9	0.77	276 $^{+79}_{-79}$	0.62	1.42	8.46	4.29	1.52	0.55
25	2.1 $^{+0.2}_{-0.2}$	2.2	1.81	4044 $^{+432}_{-432}$	1.47	1.15	11.06	5.00	1.32	0.46
26	1.7 $^{+0.5}_{-0.5}$	2.2	1.35	1982 $^{+601}_{-601}$	1.29	1.36	13.34	12.67	2.48	0.76
27	1.7 $^{+0.2}_{-0.2}$	1.7	1.37	358 $^{+247}_{-247}$	0.67	2.20	17.31	16.24	2.37	0.71

Note. Column 1: IRDC identification number; Column 2: H₂ column density matching the edge of the N₂H⁺(1–0) emission (median, 16th and 84th percentiles); Column 3: H₂ column density from which the dendrogram tree starts; Column 4: IRDC radius corresponding to $N_{\text{N}_2\text{H}^+}^{\text{start}}$; Column 5: Gas mass within $R_{\text{N}_2\text{H}^+}^{\text{start}}$, uncertainties reflect the mass changes when considering the 16th and 84th percentiles of $N_{\text{N}_2\text{H}^+}^{\text{edge}}$; Column 6: N₂H⁺(1–0) velocity dispersion estimated within $R_{\text{N}_2\text{H}^+}^{\text{start}}$; Column 7: virial ratio estimated within $R_{\text{N}_2\text{H}^+}^{\text{start}}$; Column 8: Parent cloud radius; Column 9: Gas mass within $R_{\text{CO}}^{\text{start}}$; Column 10: ¹³CO(1–0) velocity dispersion estimated within $R_{\text{CO}}^{\text{start}}$; Column 11: Virial ratio estimated within $R_{\text{CO}}^{\text{start}}$.

pixels need to be larger than the number of pixels within an angular resolution element, and need to be part of a structure whose column density amplitude from local maximum to local minimum is larger than a predefined threshold, $N_{\text{H}_2}^{\text{th}}$. The column density increment we used in our dendrogram analysis is $\sigma_{N_{\text{H}_2}} = 2 \times 10^{21}$ cm $^{-2}$ for all clouds, with $N_{\text{H}_2}^{\text{th}} = 5\sigma_{N_{\text{H}_2}}$. The starting column density contour, $N_{\text{N}_2\text{H}^+}^{\text{start}}$ (see Table 2) is set to be larger or equal to $N_{\text{N}_2\text{H}^+}^{\text{edge}}$, and is determined by eye. The reason for not systematically having $N_{\text{N}_2\text{H}^+}^{\text{start}} = N_{\text{N}_2\text{H}^+}^{\text{edge}}$ is that the $N_{\text{N}_2\text{H}^+}^{\text{edge}}$ contour can be more extended than the coverage of our N₂H⁺(1–0) maps, and therefore, in such cases, the computed masses would be overestimated. The mass of any identified group of pixels is then given by

$$M_{\text{N}_2\text{H}^+} = \Omega_{\text{pix}}^{\text{N}_2\text{H}^+} d^2 \mu_{\text{mol}} m_{\text{H}} \sum_{i=1}^{n_{\text{pix}}^{\text{N}_2\text{H}^+}} \left(N_{\text{H}_2,i} - N_{\text{N}_2\text{H}^+}^{\text{edge}} \right), \quad (1)$$

where the sum is on all the $n_{\text{pix}}^{\text{N}_2\text{H}^+}$ pixels belonging to the group of interest, $\Omega_{\text{pix}}^{\text{N}_2\text{H}^+}$ is the solid angle subtended by a pixel, d is the distance to the IRDC, μ_{mol} is the mean molecular weight and is set to

2.33, and m_{H} is the mass of the hydrogen atom. The estimated radius associated with that group is calculated via the following relation:

$$R_{\text{N}_2\text{H}^+} = \sqrt{\frac{n_{\text{pix}}^{\text{N}_2\text{H}^+} \Omega_{\text{pix}}^{\text{N}_2\text{H}^+} d^2}{\pi}}. \quad (2)$$

Projected masses estimated this way will always overestimate the mass enclosed within the volume of radius r as lower density material along the line of sight is wrongly associated with that volume (see Section 4). In Table 2, we provide the radius, mass, and aspect ratio of each IRDC at the starting column density contour $N_{\text{N}_2\text{H}^+}^{\text{start}}$. Note that we also give the mass uncertainties related to the 16th–84th percentiles range of $N_{\text{N}_2\text{H}^+}^{\text{edge}}$ values.

In order to estimate the dense gas velocity dispersion of the structures identified in the dendrogram of the *Herschel* column density images, we computed their corresponding N₂H⁺(1–0) spectra, averaged over all $n_{\text{pix}}^{\text{N}_2\text{H}^+}$ pixels that belong to the relevant group. We then used a PYTHON routine, inspired from that of GILDAS/CLASS, that uses the *curvefit* minimization routine in order to fit the 7 hyperfine components of the N₂H⁺(1–0) transition. The parameters of the fit are the central velocity $v_{\text{N}_2\text{H}^+}$, the velocity dispersion of the gas $\sigma_{\text{N}_2\text{H}^+}$,

the sum of the central opacities of the 7 hyperfine components $\tau_{\text{N}_2\text{H}^+}$, and the sum of the antenna temperature peaks of the 7 hyperfine components $T_{\text{ant}}^{\text{tot}}$. The velocity dispersion $\sigma_{\text{N}_2\text{H}^+}$ is obtained from the best fitting model. Examples of average $\text{N}_2\text{H}^+(1-0)$ and their fit are displayed in Fig. 1 for SDC18.888 (and in Appendix A for the other clouds). We fitted only one velocity component to all spectra, even for those showing potential multiple velocity components as those are almost systematically blended once the emission is averaged within each contour. The velocity dispersions $\sigma_{\text{N}_2\text{H}^+}^{\text{start}}$ estimated within the column density contour $N_{\text{N}_2\text{H}^+}^{\text{start}}$ are given in Table 2.

3.2 Diffuse gas

One key aspect of this study is to estimate cloud properties on a large range of scales. While we presented in the previous section how we estimate the properties of the clumps, we want now to connect these to their more diffuse envelopes. To achieve this, we use a combination of the *Herschel* dust continuum data and the $^{13}\text{CO}(1-0)$ GRS data (Roman-Duval et al. 2010). While the latter is primarily used to derive gas velocity dispersion, we also use it to derive the morphology of the molecular clouds along with the line-of-sight mass contamination on our *Herschel*-based mass estimates (see Fig. 2). For this purpose, we first need to compute ^{13}CO -based H_2 column density cubes.

3.2.1 ^{13}CO column density cubes

The Galactic Ring Survey $^{13}\text{CO}(1-0)$ data have been used to compute H_2 column density cubes. To do this, we followed the exact same procedure as in Roman-Duval et al. (2010). We give here a short description of this method. Towards each cloud of our sample, we compute the excitation temperature of the $^{13}\text{CO}(1-0)$ line by using the $^{12}\text{CO}(1-0)$ data from the UMSB survey and assuming that this line is optically thick. Then we make the further assumption that the excitation temperature of the $^{12}\text{CO}(1-0)$ line is the same as that of the $^{13}\text{CO}(1-0)$ line. With these assumptions, we can compute the $^{13}\text{CO}(1-0)$ excitation temperature for every voxel. In some cases, where there are strong density/temperature gradients not traced by $^{12}\text{CO}(1-0)$ (because it is optically thick) but traced by $^{13}\text{CO}(1-0)$ the estimated excitation temperature is not high enough. In such cases (~ 1 per cent of the voxels), we artificially increase the excitation temperature by 10 per cent, enough to get the excitation temperature larger than the $^{13}\text{CO}(1-0)$ brightness temperature everywhere in our cloud sample. Combining the excitation temperature with the $^{13}\text{CO}(1-0)$ cube one can compute the $^{13}\text{CO}(1-0)$ opacity which is then converted into a ^{13}CO column density, and finally into a H_2 column density assuming a constant ^{13}CO abundance with respect to H_2 of 1.8×10^{-6} for all clouds (Blake et al. 1987; Langer & Penzias 1990). This procedure provides us with cubes of H_2 column density for each IRDC. Note that some IRDCs are embedded within the same molecular clouds, and as a result we end up with 27 IRDCs embedded within 24 individual molecular clouds.

3.2.2 Mass and velocity dispersion estimates

For each molecular cloud we estimate two mass profiles, one using our *Herschel*-based column density images (see Section 3.1.1) and one using the ^{13}CO -based column density cubes. Each of them are affected by different biases that can be, at least partially, removed by using the combination of both data sets. On one hand, far-infrared dust continuum emission of Galactic plane molecular clouds is mostly optically thin and traces the entire ISM, but suffers from line-of-sight confusion (see Fig. 2). As a result, one cannot

determine correctly the morphology of the clouds using our *Herschel*-based column density images and mass estimates are likely to be overestimated. On the other hand, ^{13}CO -based column density cubes permit the identification of individual molecular clouds along the velocity axis, but can suffer from opacity effects and abundance variations. Because our mass estimates on clump scale are based on the *Herschel* column density images, we have decided to do the same for the diffuse parts of the clouds. However, we use the ^{13}CO -based column density cubes to determine their morphologies, along with determining the percentage of multiple cloud line-of-sight mass contamination in our *Herschel*-based mass measurements.

Using our ^{13}CO -based column density cubes, we first produced a 2D H_2 column density map by integrating the cube in a 5–10 km s^{-1} window centred on the cloud systemic velocity (see Fig. 1 and Appendix A). Then, we ran the same dendrogram analysis on this map as the one used on the clumps. We then produced the average ^{13}CO -based H_2 column density spectra for all identified groups of connected pixels. While the resulting spectra displayed in Fig. 1 for the SDC18.888–0.476 cloud show a relatively simple (even though non-Gaussian) single-peaked emission line, most clouds exhibit rather complex spectra often exhibiting multiple components with overlapping column density wings (see Appendix A).

With this in mind, we used multiple-Gaussian, up to a maximum of four components, to fit each spectrum using the PYTHON *curvefit* function (we also tested two other methods – see Appendix B). The mass $M_{^{13}\text{CO}}$ and velocity dispersion $\sigma_{^{13}\text{CO}}$ are then estimated using the following equations for the velocity dispersion:

$$\sigma_{^{13}\text{CO}} = \sqrt{\sum_i w_i [(v_i - \bar{v})^2 + \sigma_i^2]}, \quad (3)$$

where the sum is over the Gaussian components, and w_i , v_i , and σ_i are the weight, the central velocity, and velocity dispersion of the i th component, respectively. The centroid velocity \bar{v} is obtained by

$$\bar{v} = \sum_i w_i v_i. \quad (4)$$

And the weights are defined by

$$w_i = \frac{m_i}{\sum_i m_i}, \quad (5)$$

where m_i is the mass resulting from the integration of each individual Gaussian component, and

$$M_{^{13}\text{CO}} = \sum_i m_i. \quad (6)$$

The velocity dispersion calculated via equation (3) includes two terms, i.e. the velocity dispersion from individual Gaussian components, along with the component-to-component centroid velocity dispersion. This is justified by the fact that we are here interested in estimating the entire kinetic energy budget of the clouds we are analysing. Note also that only the Gaussian components that we believe belong to the cloud of interest are used for the determination of the mass and velocity dispersion. Those are identified by integrating, separately, each $^{13}\text{CO}(1-0)$ emission peak and visually evaluate what peak best matches the morphology of the embedded IRDC. It is possible though that different components that we consider as being part of different molecular clouds are physically interacting with each other via, e.g. cloud–cloud collision. Such interactions can lead to the creation of intermediate velocity gas (Haworth et al. 2015; Bisbas et al. 2017) for which it might become difficult to determine to which cloud it belongs, potentially leading to large uncertainties in the estimate of $\sigma_{^{13}\text{CO}}$. In Fig. 5, we show the case of SDC18.624–

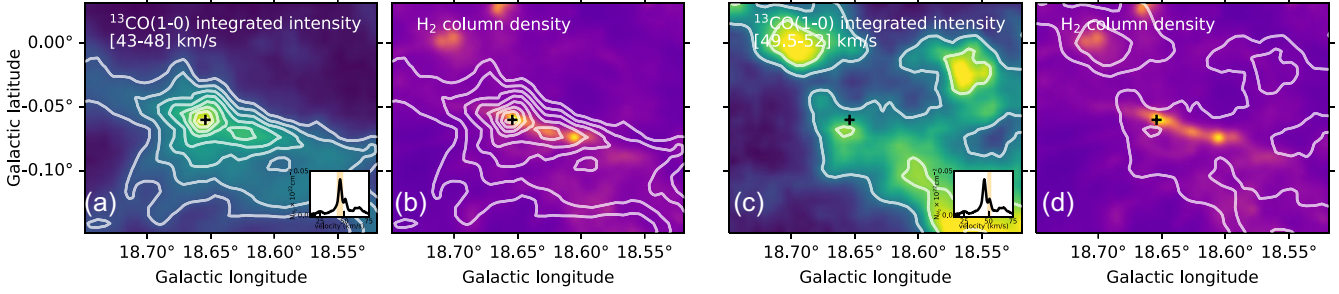


Figure 5. (a) $^{13}\text{CO}(1-0)$ integrated intensity map (colour and contours) of the lower velocity emission peak observed towards SDC18.624–0.070 at the native 44 arcsec GRS angular resolution. The plus sign shows the H_2 column density peak of the targeted IRDC. The average column density spectrum of the cloud is displayed as an inset in the bottom right corner, the orange-shaded region shows the velocity integration interval. (b) *Herschel*-based H_2 column density map at 28 arcsec resolution of the same region and same contours as in (a). (c) and (d) show the same quantities as (a) and (b) but focussed on the high-velocity emission peak observed towards SDC18.624–0.070.

0.070 for which it has been argued that such collision is currently occurring (Dewangan et al. 2018). On that figure, we display the $^{13}\text{CO}(1-0)$ integrated intensity maps in the two velocity intervals that encompass the two emission peaks present in the region. Those maps are displayed at the native 44 arcsec resolution of the GRS survey. First, we can see that the lower velocity component nicely matches the morphology of the *Herschel*-based H_2 column density obtained for that cloud, while the higher velocity component does not. This demonstrates that the gas traced by $^{13}\text{CO}(1-0)$ is clearly associated with the targeted IRDC, and it also allows us to discard unrelated velocity components. However, in the case of SDC18.624–0.070 the morphology of the higher velocity cloud does indeed suggest an interaction with the lower velocity one. A similar exercise has been made for all clouds in order to ensure the correct association of the $^{13}\text{CO}(1-0)$ components to each IRDC.

The radius of each dendrogram’s connect group of pixels is given by

$$R_{^{13}\text{CO}} = \sqrt{\frac{n_{\text{pix}}^{^{13}\text{CO}} \Omega_{\text{pix}}^{^{13}\text{CO}} d^2}{\pi}}, \quad (7)$$

where $n_{\text{pix}}^{^{13}\text{CO}}$ is the number of pixels within each connected group of pixels and $\Omega_{\text{pix}}^{^{13}\text{CO}}$ is the solid angle subtended by a pixel. In parallel to these ^{13}CO -based mass estimates, we derive *Herschel*-based ones. For this we use the exact same connected groups of pixels as those used above, but this time we use our *Herschel*-based H_2 column density maps to obtain the masses via

$$M_{\text{Hers.}}^{\text{unc}} = \Omega_{\text{pix}}^{^{13}\text{CO}} d^2 \mu_{\text{mol}} m_{\text{H}} \sum_{i=1}^{n_{\text{pix}}^{^{13}\text{CO}}} N_{\text{H}_2, i}, \quad (8)$$

where all parameters are identical to those presented in equation (1) and $M_{\text{Hers.}}^{\text{unc}}$ stands for *uncorrected Herschel*-based masses. The reason why those are uncorrected is due to the contamination of the mass estimates by the presence of multiple clouds along the line of sight. One can correct for this by estimating the fraction f_{los} of the total mass of molecular clouds along the line of sight that is locked up within the cloud of interest. That can be achieved by integrating the ^{13}CO -based H_2 column density spectra across the entire GRS velocity range, along with integrating the best-fitting Gaussian model for the cloud of interest. This can be formulated as

$$f_{\text{los}} = \frac{\int_{\text{model}} N_{\text{H}_2}^{^{13}\text{CO}} dv}{\int_{\text{all}} N_{\text{H}_2}^{^{13}\text{CO}} dv}. \quad (9)$$

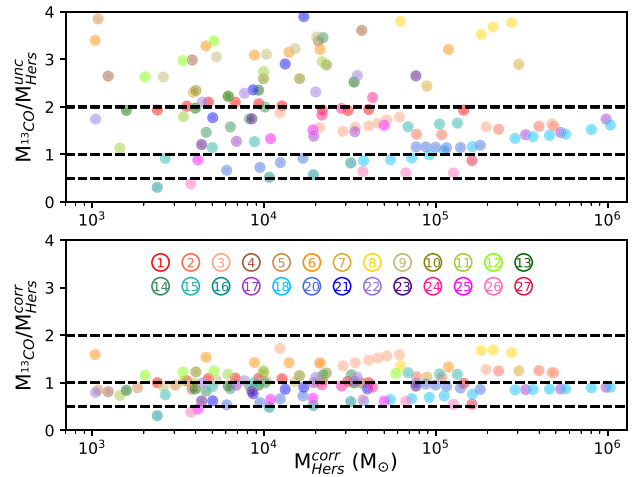


Figure 6. Comparison between the ratio of ^{13}CO -based and *Herschel*-based uncorrected/correct (top/bottom) cloud masses for all clouds, at all radii, as a function of the corrected *Herschel*-based cloud masses.

This correction factor can be calculated for each dendrogram group of connected pixels and then be applied to the uncorrected masses via

$$M_{\text{Hers.}}^{\text{corr}} = f_{\text{los}} M_{\text{Hers.}}^{\text{unc}}. \quad (10)$$

Fig. 6 shows a comparison of the ratio of $M_{^{13}\text{CO}}/M_{\text{Hers.}}^{\text{unc}}$ versus $M_{\text{Hers.}}^{\text{corr}}$ and $M_{^{13}\text{CO}}/M_{\text{Hers.}}^{\text{corr}}$ versus $M_{\text{Hers.}}^{\text{corr}}$. This figure clearly shows the vast improvement in the mass agreement once the correction factor is being applied. After correction, the masses agree within less than a factor 2 and we see little evidence for significant ^{13}CO depletion, at least not on those scales. This excellent agreement also indicates that one can safely use the $^{13}\text{CO}(1-0)$ velocity dispersion measurements in conjunction with the *Herschel*-based cloud masses. In the rest of this paper, we will be using the *Herschel*-based corrected masses.

3.3 Combined profiles

In this paper, we adopt a top-down approach by which, for every column density contours, we only analyse the one group of connected pixels that covers the position of the IRDC *Herschel*-based column density peak. As a result, sibling clumps that might be part of the same molecular clouds as our IRDC sample are not separately analysed, even though they contribute to the mass and velocity

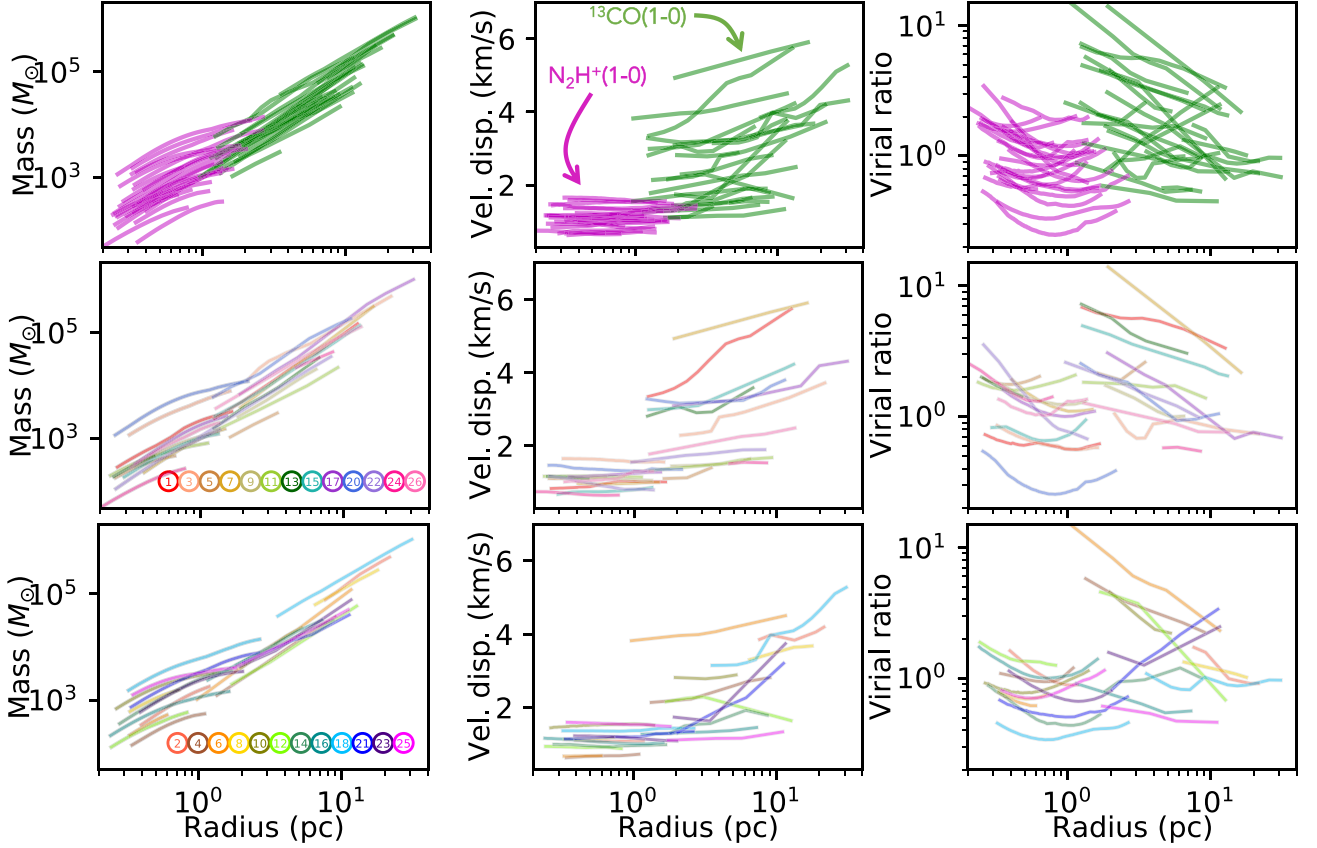


Figure 7. Profiles of all 26 IRDCs and their parent molecular clouds from our sample. On the top row, the purple points represent those for which the clump scale velocity dispersion has been measured using $\text{N}_2\text{H}^+(1-0)$, and the green points are those for which the cloud scale velocity dispersion has been measured using $^{13}\text{CO}(1-0)$. The middle and bottom rows show the same data point as the top row but each individual cloud/clump has a unique colour so that one can track their profiles. Half of the clouds have been plotted in each for clarity. Left: Mass profiles $m(r)$; middle: velocity dispersion profiles $\sigma_{\text{tot}}(r)$; right: virial ratio profiles $\alpha_{\text{vir}}(r)$.

dispersion of the dendrogram structures that encompass both them and the targeted IRDC.

Fig. 7 shows the mass profiles $m(r)$ and the velocity dispersion profiles $\sigma_{\text{tot}}(r)$ for the 26 clumps of our sample and their parent molecular clouds. For the measurement on clump scales (the purple lines) we have $m(r) = M_{\text{N}_2\text{H}^+}(R_{\text{N}_2\text{H}^+})$, while for the measurements on cloud scale (the green lines), we have $m(r) = M_{^{13}\text{CO}}(R_{^{13}\text{CO}})$. Also, the velocity dispersion σ_{tot} is the total (thermal+turbulent) line-of-sight velocity dispersion of the gas and is estimated using the observed velocity dispersion via

$$\sigma_{\text{tot}}^2 = \sigma_{\text{line}}^2 + k_B T \left(\frac{1}{\mu_{\text{mol}} m_{\text{H}}} - \frac{1}{m_{\text{mol}}} \right), \quad (11)$$

where σ_{line} is the observed velocity dispersion of the gas as inferred from the observation of a given molecular line [$\text{N}_2\text{H}^+(1-0)$ for the purple points, and $^{13}\text{CO}(1-0)$ for the green points], T is the gas temperature, m_{mol} is the mass of the observed molecule (here $m_{\text{mol}} = m_{\text{N}_2\text{H}^+} = m_{^{13}\text{CO}} = 29m_{\text{H}}$), μ_{mol} is the molecular weight which is here taken to be 2.33, and m_{H} is the mass of the hydrogen atom. We here assume a gas temperature of 15 K for all clouds, which is the average temperature measured within IRDCs (e.g. Peretto et al. 2010; Battersby et al. 2011). The impact of that assumption is negligible for most velocity dispersion measurements, and only have a measurable impact for velocity dispersions $\leq 1 \text{ km s}^{-1}$.

Finally, the right-hand panel of Fig. 7 shows the corresponding virial ratio profiles $\alpha_{\text{vir}}(r)$. Virial ratios, defined as $\alpha_{\text{vir}} = 2E_K/|E_G|$ with E_K the kinetic energy of the gas and E_G its gravitational energy, provide a zero-order measure of a cloud dynamical state. While the kinetic energy of a cloud can be relatively easily estimated, the estimate of its gravitational energy usually requires to make simplifying assumptions on the morphology and density profile of the cloud. Bertoldi & McKee (1992) have evaluated E_G in case of different power-law densities and different cloud aspect ratios. They show that for cloud with aspect ratios lower than 10 (as it is the case in this study) $|E_G|$ is only decreased by a maximum of 8 per cent compared to the spherical case. However, for clouds that have power-law density such as $\rho \propto r^{-\gamma}$ with $\gamma = 2$, $|E_G|$ is increased by 67 per cent. The impact of the density gradient on $|E_G|$ is stronger than the non-sphericity of the cloud. For simplicity, most studies of the virial ratio of molecular clouds usually approximate them as uniform density spheres, which is also what we will do, and discuss correction factors later. In this case, one can show that the virial ratio $\alpha_{\text{vir}}(r)$ is given by

$$\alpha_{\text{vir}}(r) = 5 \frac{\sigma_{\text{tot}}^2 r}{Gm}. \quad (12)$$

Fig. 7 shows a number of important features. In the following, we will discuss those separately.

3.3.1 Observed mass profiles

The mass profiles presented in Fig. 7 spread over 4 orders of magnitude in mass and 2 orders of magnitude in radius. The masses estimated on cloud scale (the green lines) and clump scale (the purple lines) mostly connect at a scale of about 2 pc, which corresponds to the maximum extent of the $N_2H^+(1-0)$ emission and half the resolution ($3'$) of the ^{13}CO -based column density images that we use to derive the morphology of the clouds. Note that, even though derived from the same *Herschel*-based H_2 column density maps, the masses on clump and cloud scales do not produce continuous mass profiles. The reason for this is that we are removing the column density background $N_{N_2H^+}^{edge}$ to every clump scale mass measurements so that the velocity dispersion estimate is that of the measured gas mass. Finally, when looking at shapes of the profiles, we notice that the clump scale mass profiles are more curvy and exhibit shallower gradients than those from the more diffuse parts.

3.3.2 Observed velocity dispersion profiles

The velocity dispersion profiles presented in Fig. 7 are the most striking. First, there is a clear discontinuity between the velocity dispersion measurements obtained on clump scale and those obtained on cloud scale. Having such different measurements clearly indicates that there is a systematic bias in the method that is being used to perform those measurements. Secondly, the shapes of the profiles are also strikingly different. While on the largest scale, the velocity dispersion mostly decreases with decreasing radius, on the smallest scale, the velocity dispersion profiles are mostly flat. This is very different from a typical Larson-type relation (Larson 1981) for which we would expect the velocity dispersion to decrease down to the sonic-scale at about 0.1 pc.

The method used to derive the velocity dispersions of the often complex $^{13}CO(1-0)$ spectra may have an impact of the observed discontinuity. As presented in Appendix B, in addition to the multiple Gaussian fitting, we also applied two other methods, i.e. a standard moment method, alongside what we call the peak method. The latter is based on the full width at half-maximum (FWHM) of the main emission peak and tends to exclude low-intensity high-velocity wings from the velocity dispersion measurements. While the moment method increases even further the discontinuity between clump and cloud scales, the peak method slightly decreases it, with a larger fraction of cloud exhibiting relatively flat velocity dispersion profiles all the way up to tens of parsecs (see Fig. B3). However, the overall behaviour of the profiles remain very similar to what is obtained when using the Gaussian fitting method.

3.3.3 Observed virial ratio profiles

Since the virial ratio profiles presented in Fig. 7 are built from the mass and velocity profiles, they carry similar features. For instance, the virial ratios present a discontinuity at the around $r = 2$ pc, which is the consequence of the discontinuity observed in the velocity dispersion profiles. Note, however, that this discontinuity is attenuated as a result of the slightly larger masses estimated from the cloud scale measurements at that radius. Also, it is pretty clear that for most of the clouds, the virial ratios on the large scales (green lines) increase as the radius decreases. This trend has already been observed by Hernandez & Tan (2015) who interpreted it as a sign of CO depletion. Finally, the virial ratios estimated on clump scales

(purple lines) present a curvy shape, which is the direct reflection of the curvy mass profiles observed on the same scales.

3.4 Uncertainties

There are a number of uncertainties that we need to consider when interpreting the profiles presented in Fig. 7. First, there are uncertainties that do not affect the shape of the profiles but do impact their overall scaling. One example of such uncertainty is the distance to the clouds which is typically 10–20 per cent (Reid et al. 2009). If our IRDC-hosting cloud are not located at the near distance though then the distance could be 4 times larger for some clouds (see Fig. F1). That uncertainty will impact the mass and radius measurements uniformly across the profile of an individual cloud. Secondly, there are uncertainties that can potentially impact the shape of individual profiles. Regarding the mass profiles, the assumption of a single temperature along the line-of-sight could potentially have an impact on the shape of the observed profiles. However, as we have shown in Section 3.1.3, the impact on the shape of the profile is minimal, while the impact on the absolute mass values can be impacted by 20 per cent on average. Another uncertainty is related to the dust emissivity, i.e. κ_λ , we used when computing the *Herschel*-based H_2 column density maps. In this study, we used the same dust emissivity law for the clump scale and cloud scale measurements. It is however well known that dust emissivity changes with density and temperature (e.g. Ysard et al. 2015; Sadavoy et al. 2016). At this point, we have no means to set strong constraints on this particular aspect of dust property uncertainties, but the law we adopted has been shown to be compatible with dust emission in both the more diffuse (Planck Collaboration XXV 2011) and denser (Rigby et al. 2018) gas environments. Also, as it can be seen in Fig. 6, the *Herschel*-based masses are within a factor of two of the ^{13}CO -based masses which use a completely different set of assumptions. This suggests that, if dust properties do change across the radial profiles of molecular clouds, this does not have a dramatic effect on our mass estimates. Finally, the uncertainty related to our choice of $N_{N_2H^+}^{edge}$ (see Section 3.1.3) has a direct impact on the clump scale mass estimates with a ~ 10 per cent to ~ 30 per cent uncertainty for most clumps (see Table 2). This fractional mass uncertainty is not constant across the clump radial profiles and therefore can affect the mass profile shape. However, after computing the clump mass profiles with a representative range of $N_{N_2H^+}^{edge}$ we can confirm that their overall shapes are barely affected (see Appendix C for the special case $N_{N_2H^+}^{edge} = 0$).

Regarding uncertainties on the velocity dispersion, the $N_2H^+(1-0)$ and $^{13}CO(1-0)$ measurements differ. Indeed, the $N_2H^+(1-0)$ velocity dispersion measurements are very well constrained, and have uncertainties that are of the order of ~ 0.1 km s $^{-1}$. This implies that the flat velocity dispersion profiles observed on clump scale are very robust. Uncertainties on the $^{13}CO(1-0)$ velocity dispersion measurements are a lot more variable from cloud-to-cloud depending on how complex the $^{13}CO(1-0)$ spectra are. For the simple cases, such as SDC18.888–0.476 (see Fig. 1), the uncertainty is of the order of ~ 0.2 km s $^{-1}$; however, this can be as high as ~ 1 km s $^{-1}$ in more complex cases such as SDC18.624–0.070 (see Fig. A1). These larger uncertainties are also reflected by the large differences in velocity dispersion measurements when using different evaluation methods (see Fig. B2).

Overall, while the inherent uncertainties on the different quantities presented in Fig. 7 might shift the profiles up and down, their shapes are fairly robust and are likely to be a true representation of how

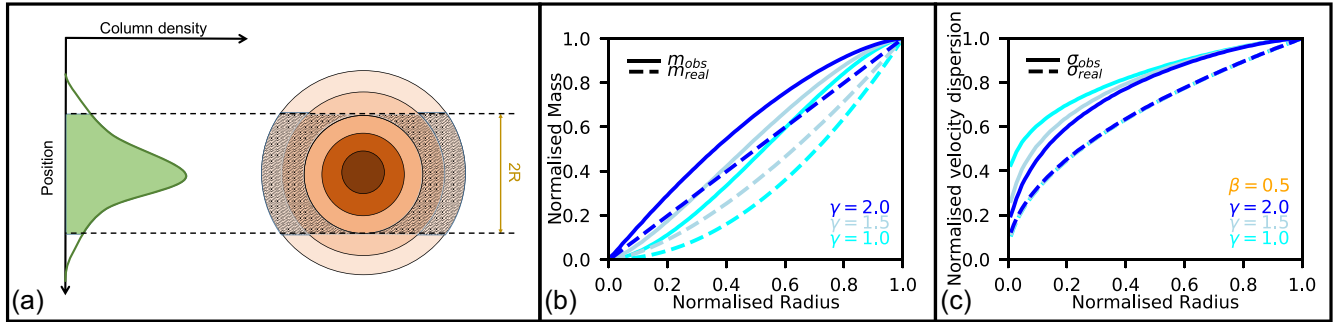


Figure 8. (a) Sketch illustrating measurement biases once a 3D cloud is being projected onto the plane of sky. In this case, a spherical cloud (on the right) whose volume density increases towards the centre has a projected column density profile that is represented by the plot on the left. The bijective mass estimate within projected radius R will be that represented by the green-shaded area, which includes material that is not part of the volume of the sphere of radius R (region of the cloud that is barred). (b) Normalized mass profiles of a spherical cloud with three different density profile $\rho \propto r^{-\gamma}$, with $\gamma = (2.0, 1.5, 1.0)$. The solid lines show the masses as observed, while the dashed lines show the real mass enclosed within a given radius. (c) Normalized velocity dispersion profiles of a spherical with the same density profiles as in (b) and with a velocity dispersion profile $\sigma \propto r^{\beta}$ with $\beta = 0.5$.

the projected mass, velocity dispersion, and virial ratio profiles of clumps and clouds behave.

4 SPHERICAL MODELS

As discussed above, the profiles displayed in Fig. 7 present a number of characteristic features. Before interpreting them one needs to be aware a few biases that exist and that we may be able to quantify. First, masses, as presented in the left-hand panel of Fig. 7, have been computed using the bijective mass estimates (Rosolowsky et al. 2008). Such masses are always overestimated as a consequence of cloud material lying along the line-of-sight which is not part of the closed volume of radius r (see Fig. 8). The impact of using the bijective method to estimate masses at different radius is illustrated in Fig. 8(b). Secondly, the velocity dispersion measurements are being done on spectra that also include the same unrelated line-of-sight material which may have larger or smaller velocity dispersion than the gas lying within the volume of interest. Depending on the exact shape of the combined density and velocity dispersion profiles, this might lead to over or underestimated observed velocity dispersions (see Fig. 8c). Also, the clump and cloud scale measurements are derived at different angular resolutions, and a background column density has been subtracted to the former and not to the latter. The impact of all those on the observed profiles is unclear. The purpose of the models presented in the rest of this section is to quantify the impact of projection on the mass and velocity dispersion measurements in relation to the observed profiles (for a similar approach on core scale see Singh et al. 2021). We do not attempt to fit the profiles of individual clouds as spherical clouds are not a good representation of the complex density structures of molecular clouds.

4.1 Single power-law profiles

We first consider models with single density and velocity dispersion power-law such as

$$\rho(r) = \rho_0 \left(\frac{r}{r_0} \right)^{-\gamma}, \quad (13)$$

$$\sigma(r) = \sigma_0 \left(\frac{r}{r_0} \right)^{\beta}, \quad (14)$$

where ρ_0 , r_0 , and σ_0 are normalization constants. For a given pair of γ and β values, we numerically construct a spherical cloud of a

given mass and radius that we then project on the plane-of-the-sky in order to construct mass surface density maps (see Appendix D for more details). We do this last operation twice, once up to radius $R_{\text{end}}^{13\text{CO}}$ and once up to radius $R_{\text{end}}^{\text{N}_2\text{H}^+}$, $R_{\text{end}}^{13\text{CO}}$, and $R_{\text{end}}^{\text{N}_2\text{H}^+}$ being the radii at which $^{13}\text{CO}(1-0)$ and $\text{N}_2\text{H}^+(1-0)$ emission becomes undetectable.¹ We then convolve each mass surface density images at the resolution of our observations. Finally, we integrate both mass surface density images at various radii to derive their projected mass profiles. Regarding the velocity dispersion profile, we first weight the velocity dispersion at each radius, in 3D, by the local mass density. We then project this quantity on to the plane of the sky, and then integrate the resulting maps at various radii. Finally, we divide these profiles by the corresponding mass profiles in order to obtain projected mass-weighted velocity dispersion profiles.

In the models presented here, there are essentially four free parameters, i.e. γ , $R_{\text{end}}^{\text{N}_2\text{H}^+}$ ($=r_0$), $R_{\text{end}}^{13\text{CO}}$, and $M_{\text{end}}^{\text{N}_2\text{H}^+}$, for the mass profiles, and an additional two free parameters, i.e. β , and $\sigma_{\text{end}}^{\text{N}_2\text{H}^+}$ ($=\sigma_0$), for the velocity dispersion profiles. The parameter ρ_0 is derived from γ , $R_{\text{end}}^{\text{N}_2\text{H}^+}$, and $M_{\text{end}}^{\text{N}_2\text{H}^+}$ and is, thus, not a free-parameter of the models. As already mentioned, the purpose of those models are not to find a set of best parameters for each individual clouds, but rather to understand the trends that are present in the cloud sample. With that in mind, Fig. 9 shows a set of 9 models against the observed profiles. The normalization of those models is such they match the range of mass and velocity dispersion at parsec scales. Each row corresponds to a different γ value but the same β value. In each row, the three panels correspond to the mass, velocity dispersion, and virial ratio profiles. There are a number of important features in those models that we can notice straight away. First, regarding the mass profiles, one can see that the cases $\gamma = 1$ and $\gamma = 2$ overpredict and underpredict, respectively, the mass of the clouds on the largest scales. We also notice that, while the $\gamma = 1.5$ case provides a better overall agreement with the observed profiles, the profile shapes provided by the cases $\gamma = 2$ and $\gamma = 1$ seem to give a better match to the inner and outer parts, respectively, of the observed profiles. We also notice that we successfully reproduce the curved shape of the inner parts of the profiles.

¹Note that the R_{end} parameters are defined pre-convolution and as such do not exactly match the R_{edge} parameters defined in Section 3 that are obtained directly from the observations (i.e. post-convolution).

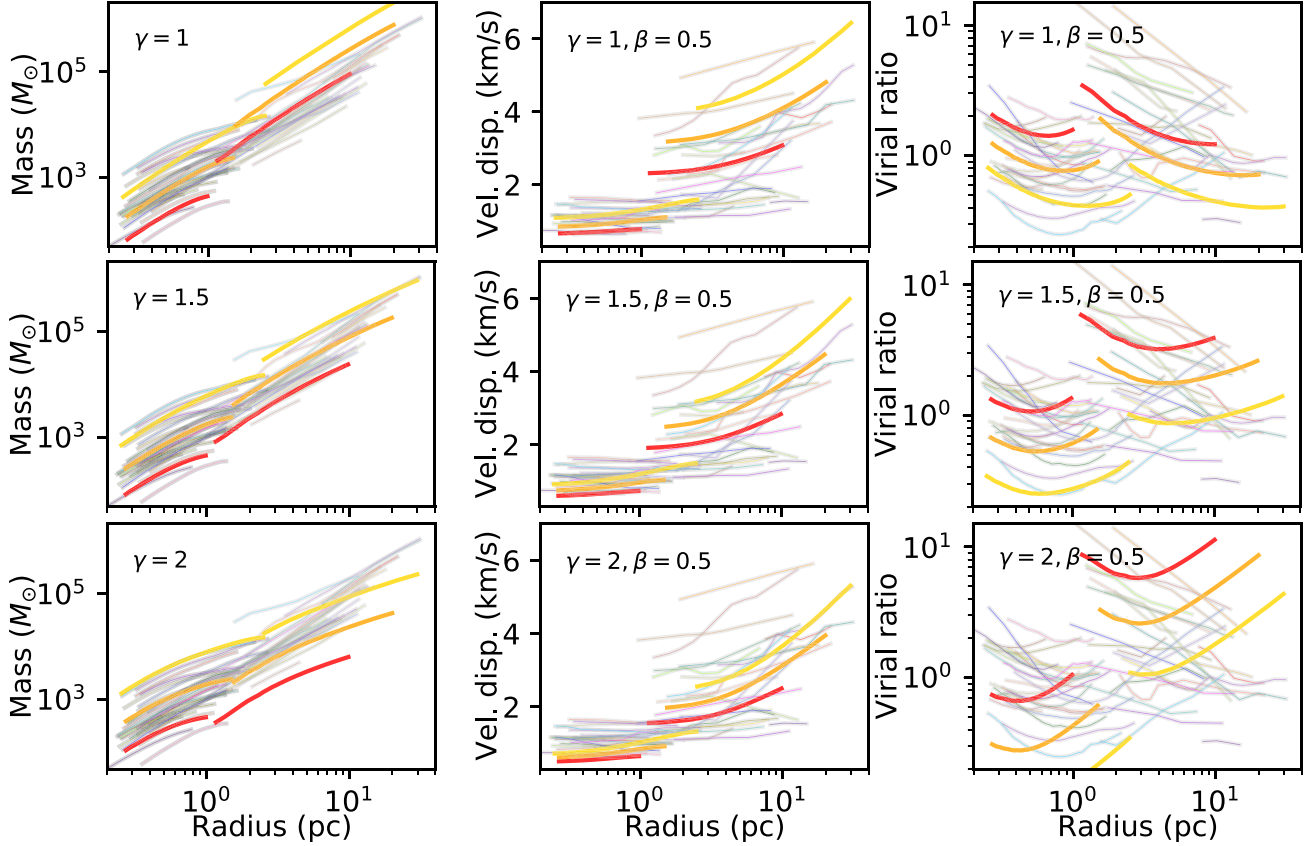


Figure 9. Mass, velocity dispersion, and virial ratio profiles (from left to right), for three different γ values (from top to bottom: $\gamma = [1.0, 1.5, 2.0]$). The grey lines are the same observed data points as presented in Fig. 7. The red, orange, and gold lines are three different spherical models with three different normalizations such that they cover the range of masses and velocity dispersions as measured on parsec scale (i.e. on scales representative of $R_{\text{N}_2\text{H}^+}^{\text{start}}$ in Table 2). All models have the same velocity dispersion profile exponent, i.e. $\beta = 0.5$.

Moving on to the velocity dispersion profiles displayed in Fig. 9, it is clear that the simple 1D models represented here manage to reproduce the velocity dispersion discontinuity, in particular for the $\gamma = 1$ case. The reason for this is that, for that series of models, a larger fraction of the mass is at low density where the velocity dispersion is the largest and as a result of the projection, the mass weighted velocity dispersion is overestimated by a large factor, up ~ 3 in the $\gamma = 1$ case. Also, while the $\gamma = 1$ case manages to reproduce in a satisfactory way the shape and amplitude of the outer velocity dispersion profile, it cannot entirely match the observed flat velocity dispersion profiles in the inner regions. And this gets worse when considering steeper density profiles, i.e. $\gamma = 1.5$ and $\gamma = 2$.

Finally, looking at the virial ratio profiles in the last column of Fig. 9, we notice that none of them are completely satisfactory when compared to the observed profiles, even though one could argue that the shallower density models do better than the steeper ones.

From this comparison between single power-law models and observed profiles, it seems clear that most of the observed features can be reproduced, at least to some extent, providing strong evidence that projection biases are mostly responsible for them. This comparison also shows that the single power-law models are limited and do not allow us to reproduce both the inner and outer parts of the observed mass and velocity dispersion profiles. Most noticeable is the velocity dispersion profiles for which the flat inner profiles are clearly different from the outer profile shapes.

4.2 Broken power-law profiles

In this section, we extend the models presented above from single power-law profiles to broken power-law profiles. More explicitly, we set two power-law exponents for both the density and velocity dispersion profiles defined as

$$\gamma_{\text{in}} \text{ and } \beta_{\text{in}} \text{ for } r < r_0 \quad \gamma_{\text{out}} \text{ and } \beta_{\text{out}} \text{ for } r > r_0. \quad (15)$$

The method used to create the profiles is identical to that presented in the previous section. Based on our single power-law models, it seems that the inner density profiles are, on average, steeper than the outer ones. Therefore, in the series of models presented in Fig. 10 we used $\gamma_{\text{in}} = 2$ and $\gamma_{\text{out}} = 1.5$. Regarding the velocity dispersion profiles it seems clear that the velocity dispersion on clump scale is rather flat, with apparent very little variation in the profiles. On the other hand, the velocity dispersion profiles on cloud scale are diverse, both in terms of shape and normalization. Therefore, each row in Fig. 10 corresponds to a different value of β_{out} , while β_{in} is fixed to 0 for all models. In that figure one can see that we now reproduce rather well the average shape and magnitude of the mass profiles, and similarly for the velocity dispersion profiles on clump scales. One can also see that we do reproduce well some of the velocity dispersion profiles on cloud scale, although we fail in reproducing the low-mass high-velocity dispersion profiles that populate the top part of the velocity and virial ratio profiles. This is where our simple 1D models reach their limitations. Indeed, if one looks at the large-scale

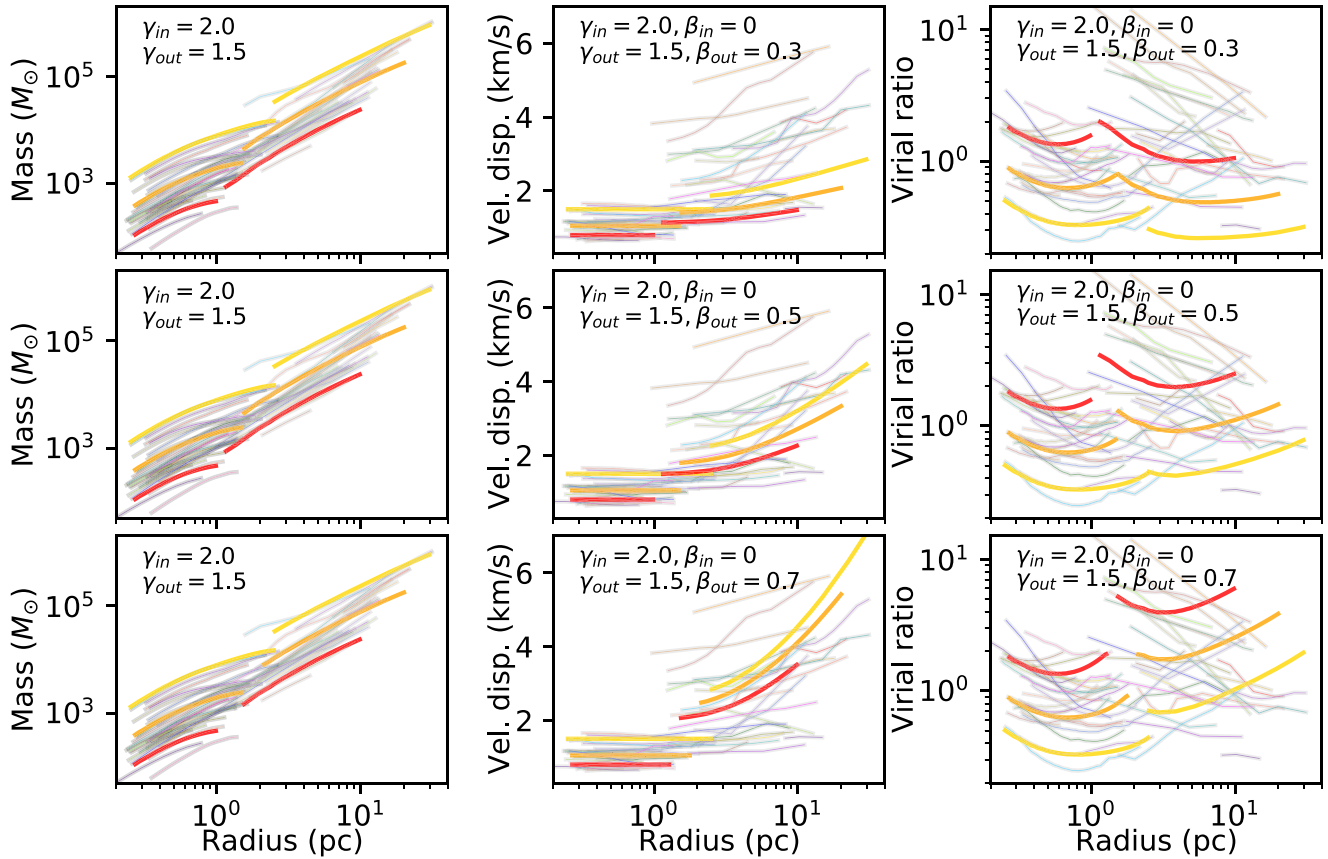


Figure 10. Same as Fig. 9 but for broken power-law profiles. Each row now corresponds to a different β_{out} value (from top to bottom: $\beta_{\text{out}} = [0.3, 0.5, 0.7]$). For all models, β_{in} , γ_{in} , and γ_{out} are fixed to $[0.0, 2.0, 1.5]$, respectively.

mass distribution of those clouds (via the ^{13}CO -based H_2 column density maps – see Fig. 1 and Appendix A), one can see that the clump we are focussing on does not dominate the mass on those scales, with many or more sibling clumps being present in the same parent cloud. As a result, the large scale velocity dispersion measured towards the clumps of interest is most likely driven by the presence of its siblings. This cannot be reproduced with spherical models. Nevertheless, what this is showing is that lower gas density layers of high-velocity dispersion gas surrounds those clumps, generating steep velocity dispersion discontinuities in their profiles.

4.3 Projected versus true profiles

In the previous subsections, we have characterized the origin of observed profile features with the help of projected models. We have not yet evaluated how the profiles of those same projected models compare to their own input profiles. Such comparison can be useful when it comes to understanding the impact of different aspects of the projection process has on the observed absolute profile values.

Fig. 11 shows the ratio of the true mass, velocity dispersion, and virial ratio profiles over those observed at 3 arcmin resolution, for all single power-law models presented in Figs 9. We focus on the cloud-scale profiles since the conclusions are the same for the clump-scale part of the models. One can see that, with the exception of the mass profile $\gamma = 2$ (see below), the observed values are nearly systematically overestimated, whether it is mass, velocity dispersion, and virial ratios. However, regarding the virial ratio profiles, one can

see that the observed values are within 20 per cent of the true value except for the inner radii, when one gets within a couple of angular resolution elements.

Often in the literature one finds that radii of structures are being deconvolved from the beam size of the telescope. This is a valid approach, particularly for point-like sources as the measured fluxes come from a region of the sky that is necessarily smaller than what is observed after beam convolution. However, when dealing with molecular cloud measurements, the picture is not that clear as, at least in our case, two competing effects come into play: beam convolution and projection effects. While for a centrally concentrated density profile beam convolution will tend to spread the flux and mass to larger radii, the line-of-sight integration of flux that does not come from within the volume of interest will tend to increase the flux/mass at a given projected radius. In Fig. 11 (left), one can see that the relative impact of both effects depends on the density profile index and radius, convolution having the strongest impact for $\gamma = 2$ at small radii resulting in mass underestimation, while projection tends to overestimate masses for any other combination of radius and γ . It thus becomes clear that projection is the dominant factor in terms of mass estimates accuracy.

We have to note here that the direct comparison of our observed profiles with the modelled ones assumes that the tracers we use (i.e. dust continuum, $^{13}\text{CO}(1-0)$, and $\text{N}_2\text{H}^+(1-0)$ emission) reliably trace the energetics of the underlying clouds. In order to show that this is the case, radiative transfer calculations of our 1D models would have to be made. While this is deferred to a future paper that will

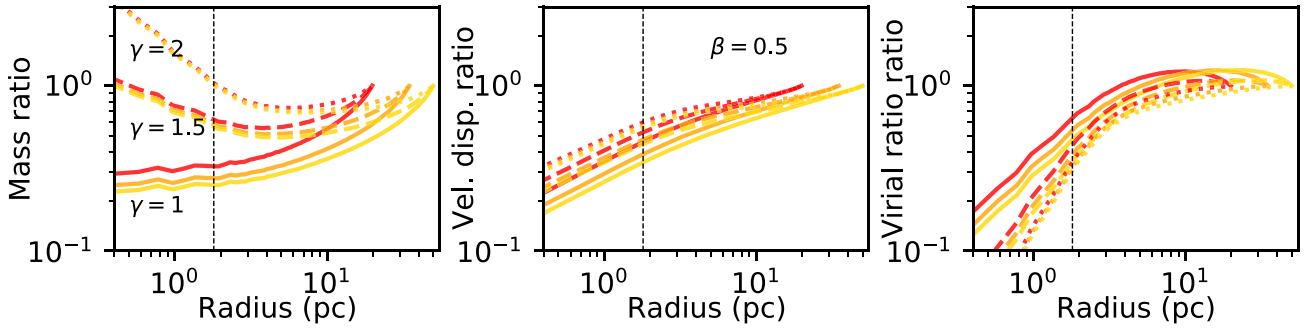


Figure 11. Ratios of the true over projected mass, velocity dispersion, and virial ratio profiles for all nine models displayed in Fig. 9. The projected models are at the same angular resolution as our ^{13}CO -based column density maps, that is 3 arcmin. The solid, dashed, and dotted profiles correspond to the density profile indices $\gamma = [1, 1.5, 2]$, respectively. All models have the same velocity dispersion profile index $\beta = 0.5$. The three colours correspond to different normalizations. The vertical black dashed line shows half of the 3 arcmin beam size at a distance of 4 kpc.

look into a larger range of tracers, we argue that the large number of similarities between observed and modelled profiles is already evidence that the combination of tracers we use here is good enough for the purpose they serve.

5 DISCUSSION

5.1 Self-gravitating molecular clouds

The question of the gravitational binding of molecular clouds has been, and still is, the subject of numerous debates (e.g. Heyer et al. 2009; Ballesteros-Paredes et al. 2011; Dobbs, Burkert & Pringle 2011; Miville-Deschênes et al. 2017; Vázquez-Semadeni et al. 2019). Here, we have all the necessary information to check whether the clouds we selected are consistent with being gravitationally bound or whether there is a scale at which they switch from being bound to unbound. The profiles displayed in Fig. 7 show that observed virial ratios for our cloud sample are nearly systematically below $\alpha_{\text{vir}} = 3$ at all radii. Most of the exceptions correspond to the measurements made at the smallest radii of the $^{13}\text{CO}(1-0)$ -based profiles. As our models showed (see Fig. 9) increased virial ratios with decreasing radii can be reproduced when large layers of high velocity dispersion gas lay along the line of sight and contaminates the measurements. As a result the most reliable measurements are those obtained on the largest scales (see Fig. 11). Fig. 12 shows the distributions of virial ratios obtained at those largest scales for both $\text{N}_2\text{H}^+(1-0)$ and $^{13}\text{CO}(1-0)$ measurements.

For uniform density spheres, the transition between gravitationally bound and unbound gas occurs at $\alpha_{\text{vir}} = 2$, while for clouds with density profiles such as $\rho \propto r^{-1}$, $\rho \propto r^{-1.5}$, and $\rho \propto r^{-2}$, the limit moves up to 2.2, 2.5, and 3.3, respectively. Correction factors regarding the non-spherical shape of clouds are less than 8 per cent as long as the aspect ratio of the clouds is lower than 10 (Bertoldi & McKee 1992), which is the case for all clouds in the sample. For non-uniform velocity dispersion profiles correction factors also exist (Miville-Deschênes et al. 2017), but these are of the order of 5 per cent for the diffuse parts of the cloud and non-existent for the dense part (see Appendix E). Fig. 12 reveals that ~ 85 per cent of ^{13}CO -based measurements, and 100 per cent of the N_2H^+ -based measurements have $\alpha_{\text{vir}} \leq 2.5$.

Virial ratios as estimated here only include the kinetic and gravitational energy volume terms of the virial theorem. However, the surface terms can also be important to consider when evaluating

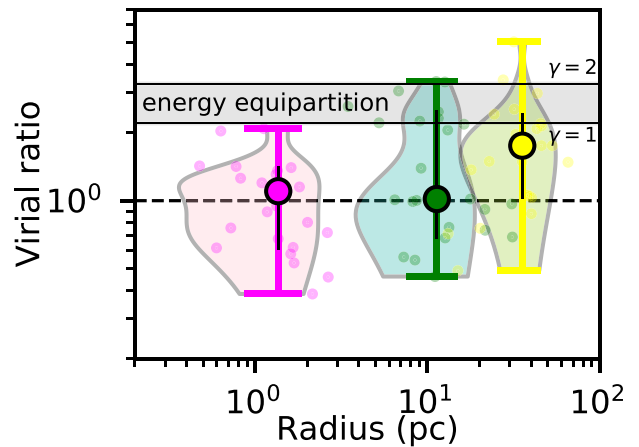


Figure 12. Violin plots of the virial ratios obtained on the largest scales in both $\text{N}_2\text{H}^+(1-0)$ (magenta) and $^{13}\text{CO}(1-0)$ (green), along with that obtained by Miville-Deschênes et al. (2017) in $^{12}\text{CO}(1-0)$ (yellow) for the same sample of clouds. Each violin plot is located, along the x-axis, at the median radius value of each group. The median virial ratio value for each group is represented by a coloured circular symbol with a black edge, while the 16th and 84th percentile ranges are represented by vertical solid black lines. We have also overplotted the corresponding individual measurements as coloured circular symbols. The horizontal black dashed lines show virial ratio values $\alpha_{\text{vir}} = 1$ while the shaded area show the region of energy equipartition for density profile indices between $\gamma = 1$ and $\gamma = 2$.

whether a piece of molecular gas is gravitationally bound or not. Dib et al. (2007) showed that, in the context of magneto-hydrodynamical simulations of turbulent molecular clouds, the surface kinetic energy of cores can be as large as its volume counterpart and be responsible for tearing them apart despite having, sometimes, virial ratios consistent with being self-gravitating. By applying a similar approach to their own simulations, Weis et al. (2022) also showed that clumps' surface terms can be significant and even govern their dynamical evolution, although clumps that are dense and massive enough to form cores have dominant volume terms and mostly self-gravitating virial ratios. Measuring the surface terms of observed clumps is, in practice, impossible since one only gets to measure cloud properties once projected onto the plane of the sky. However, by measuring virial ratios at different radii within clouds we ensure that the surface kinetic energy at a given radius becomes part of the volume kinetic

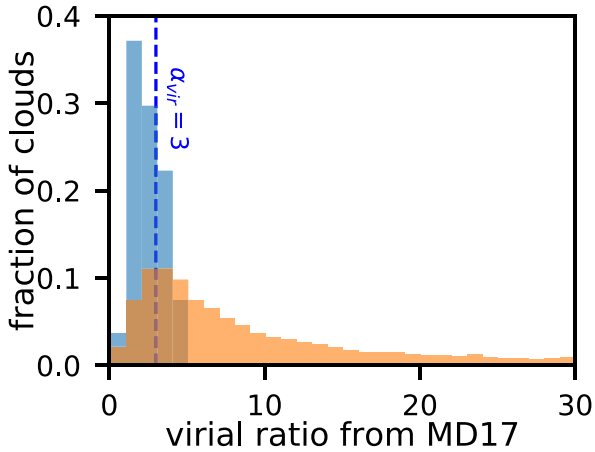


Figure 13. Distributions of virial ratios as estimated by Miville-Deschênes et al. (2017) for the 24 clouds presented here (blue histogram) and their entire cloud population (orange histogram).

energy at larger radii. As a result, virial ratio profiles of unbound clouds with large surface kinetics energy terms should exhibit self-gravitating virial ratios only at a minority of radial points. Hence, the fact that the observed virial ratios of our clump and molecular cloud sample are consistently below 3 across a large range of spatial scales (see Fig. 12) strongly supports the idea that the vast majority of the molecular clouds, if not all, is self-gravitating from tenths of a parsec up to several tens of parsecs.

How does this fit with studies such as that of Miville-Deschênes et al. (2017, MD17 hereafter), claiming that most molecular clouds are unbound? In order to answer that question we searched for the MD17 counterparts of all 24 molecular clouds from our sample and compared the distributions of the virial ratio (as estimated by MD17) to the entire MD17 cloud population. Fig. 13 shows that our 24 IRDC-hosting molecular clouds are amongst the most gravitationally bound clouds from the MD17 sample, oversampling the low virial ratio tail of the distribution. So the fact that all the clouds studied in the present paper are gravitationally bound is not in contradiction with the MD17 results. We also notice that the virial ratio values plotted in Fig. 13 and estimated by MD17 are larger than those we have estimated ourselves for the same sample of clouds. This difference could be real as MD17 computed their cloud properties from a lower gas density tracer, that is $^{12}\text{CO}(1-0)$, or it could be due to systematics in the way properties are calculated. We investigated this by reporting

the MD17 values of radius, mass, velocity dispersion, and virial ratio for all 24 clouds and added them to our observational profiles. Fig. 14 (transparent orange circular symbols) shows an overall good agreement between our data points and those from MD17. However, while the radii reported by MD17 are larger, the masses are very similar to those we report on smaller radii. The much larger angular resolution of the data used by MD17 (i.e. 8.5 arcmin) means that their radii (and thus virial ratios) might be artificially increased compared to the values derived here by us. However, since $^{12}\text{CO}(1-0)$ is a lower density tracer than $^{13}\text{CO}(1-0)$, we do expect the MD17 counterparts to have larger radii. This therefore suggests that either we have overestimated our masses or MD17 have underestimated their ^{12}CO masses. In MD17, they used a standard $X_{\text{CO}} = 2 \times 10^{20} \text{cm}^{-2} (\text{K km}^{-1})^{-1}$ factor to convert integrated ^{12}CO intensities into H_2 column densities. As Barnes et al. (2015) showed, this standard conversion factor typically underestimates column densities by a factor of ~ 2 for resolved molecular clouds. Taking into account this change in X_{CO} would put the MD17 masses more in line with ours (see Fig. 14 yellow circular symbols). In addition to this mass correction, one can wonder whether one should apply one to velocity dispersion measurements as well. Indeed, $^{12}\text{CO}(1-0)$ is typically optically thick above H_2 column densities of few 10^{20}cm^{-2} , which means that mass and velocity dispersion measurements could be overestimated and underestimated, respectively. The effect on the velocity dispersion though is probably only of the order of 20 per cent (e.g. Hacar et al. 2016), but as the result of the σ^2 dependency of the virial ratio, a small correction factor on the velocity dispersion can lead to a significant difference on the virial ratios. However, as it can be seen in Fig. 14, the velocity dispersion measurements obtained by MD17 are in good agreement with ours, and we therefore do not believe that there is a systematic underestimation of ^{12}CO velocity dispersion for the clouds we are looking at. The corresponding distribution of virial ratios has also been reported on to Fig. 12 showing that 85 per cent of the ^{12}CO -based virial ratio measurements are below 2.5, which is identical to the ^{13}CO -based virial ratio measurements. Overall, Figs 14 and 12 show that even on scales of 100 pc, the vast majority of clouds from our sample have virial ratios that are consistent with being self-gravitating.

5.2 Larson’s, Solomon’s, and Heyer’s relations

Probably one of the most influential studies on the observational characterisation of dynamical state of molecular clouds is that by Richard Larson in 1981. In that study, they found, mostly from using $^{13}\text{CO}(1-0)$ data from the literature at the time, that the averaged cloud properties follow a number of relationships such

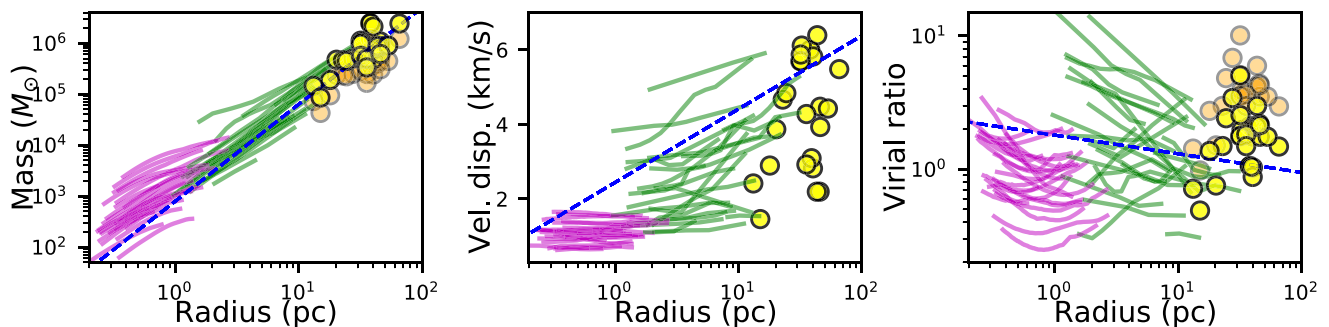


Figure 14. The profiles are the same as those presented in the upper row of Fig. 7. In addition, we have added the $^{12}\text{CO}(1-0)$ data points as presented in MD17 (transparent orange symbols) and once corrected by a factor of 2 in mass (yellow symbols). The blue dashed-lines show Larson’s laws.

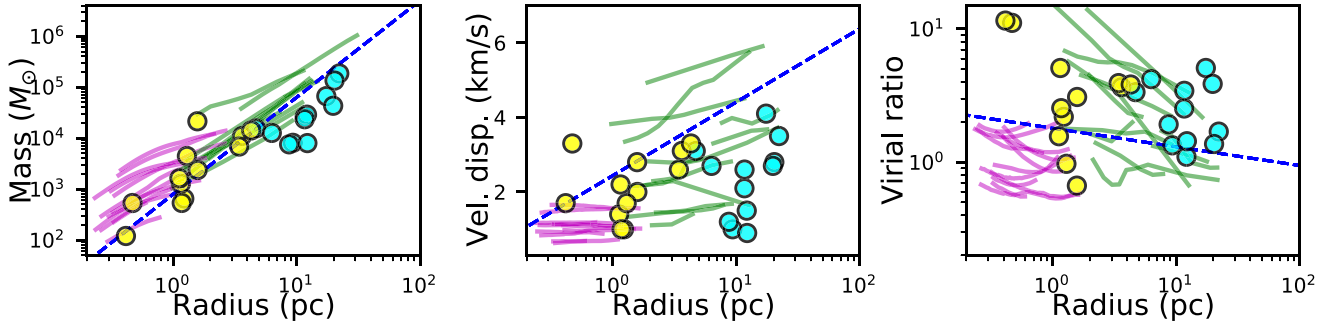


Figure 15. The profiles are the same as those presented in the upper row of Fig. 7, only restricted to the 12 clouds in common with H09. In addition, we have added the H09’s measurements for these 12 clouds, for both radii measurements. We also overplot Larson’s relations as dashed blue lines, and Solomon’s size–velocity dispersion relation in the middle panel.

that: $\sigma \propto r^\beta$ with $\beta = 0.38$, and $\rho \propto r^{-\gamma}$ with $\gamma = 1.1$. A third relation, consequence of the first two, is that molecular clouds have virial ratios close to unity and $\alpha_{\text{vir}} \propto r^{-\delta}$ with $\delta = 0.14$. Larson’s size–velocity dispersion relation has been interpreted as an evidence for turbulence-regulated gas dynamics, since $\beta = 1/3$ is what one expects for incompressible Kolmogorov-like turbulence. However, these relations have later been revised by Solomon et al. (1987, S87 hereafter) who found a steeper size–velocity dispersion relation with $\beta \simeq 0.5$. They suggested that such index is the direct consequence of the virialization of individual molecular clouds at nearly constant mass surface densities. Heyer et al. (2009, H09 hereafter) reanalysed S87 cloud sample using $^{13}\text{CO}(1-0)$ GRS data and determined that, even though cloud properties are compatible with being in virial equilibrium at all radii, the change in the internal mass surface density of clouds result in a different size–velocity dispersion relation to that proposed by Larson’s and Solomon’s.

Finding out how our study compares to those mentioned above and understanding where the differences come from is fundamental if one wants to settle the question of the dynamical states of molecular clouds. Interestingly, half of our cloud sample (12/24) is common to both H09 and S87’s samples, and since H09 used the same ^{13}CO data we use here, one can make a direct one-to-one comparison. The first property we compare is the distance used for all 12 clouds. As it can be seen in Fig. F1, for half of the clouds the distances match, while for the other half they do not. The latter group of clouds have been assigned the far distance by S87 and H09. Even though they have recalculated the kinematics distances, H09 have kept the near/far distance ambiguity solutions provided by S87. Looking in detail, these 6 clouds with far distances have been assigned so based on the fact that (i) they best fit the S87 size versus velocity dispersion relation and (ii) they best match the scale height of the molecular layer for that position and velocity range. These are both very questionable criteria. All clouds here host IRDCs, and it has been shown that 90 per cent of IRDCs are located at the near distance (Ellsworth-Bowers et al. 2013). This would suggest that maybe one of the 12 clouds presented here is indeed at the far distance, but it is very unlikely that the 6 are. In the rest of the comparison, we set the distance to all 12 clouds to that we give in Table 1.

Fig. 15 compares the profiles of the 12 clouds as we measured them with H09’s measurements (after distance correction). In H09, each cloud has two measurements taken at different radii, both measured using ^{13}CO . The cyan symbols represent the large scale measurements and the yellow symbols the small scale ones. Compared to our measurements of the same clouds, we can see that, at large radii, both H09’s masses and velocity dispersions tend to

be underestimated. On small scales though, the masses are similar but the velocity dispersions are overestimated. Before interpreting these discrepancies, one needs to understand the differences in the measurements themselves. For the large-scale mass measurements H09 used the original rectangular boxes that S87 used to measure their own masses. Those boxes were defined based the location and extent of the $^{12}\text{CO}(1-0)$ emission peaks derived from low-resolution high-noise maps. Fig. 16 show three representative examples of such boxes overlaid on top of the cloud column density images. One can see that, with the exception of the biggest clouds, the boxes do not match the cloud morphologies, sometime missing the column density peaks, and often covering regions where no, or little, column density is present. The net impact of this is, for a given effective radius (defined as the radius of the disc having the same area as the box), the mass is heavily underestimated. This problem mostly disappears for small-scale mass measurements as H09 have for those used the contours of the column density maps (as we did). Regarding the velocity dispersion measurements on small scales, H09 overestimate them as a result of the same projection effect that is responsible for overestimating our own ^{13}CO velocity dispersion measurements. On large scale, H09 underestimates the velocity dispersion most likely because of the unadapted velocity window used to compute their first-order moment. However, we cannot test this since velocity windows used for the integration by H09 are not provided.

One particular plot that has been used by H09, and many others since, to support the picture of virialized clouds on all scales is one that plots the mass surface density Σ_{gas} of the clouds versus the parameter $p = \sigma_v / \sqrt{R}$. On the left-hand panel of Fig. 17 we reproduced the figure from H09, the clouds in common with our studies being highlighted with different colours (cyan and yellow) and with black edges. In this panel, it is quite clear that the large-scale data points (the blue squares) are at lower mass surface densities than the small-scale points (orange). The distribution of these points stretch across more than two orders of magnitude along lines of constant virial ratios between 1 and 3. On the same figure, the right-hand panel shows the same quantities for the common sample of clouds with properties as derived in this paper (here we used the values displayed in Table 2). We can see that the large-scale points (green) completely overlap with the small-scale points (magenta). When compared with Heyer’s quantities for the same clouds we see that the spread is reduced by one order of magnitude. This is a direct consequence of the measurement biases explained above. In fact, whether we look at the large-scale measurements obtained on scales of 20–60 pc or measurements obtained on scales between 1.5 and 5 pc, the data points are located within a very similar

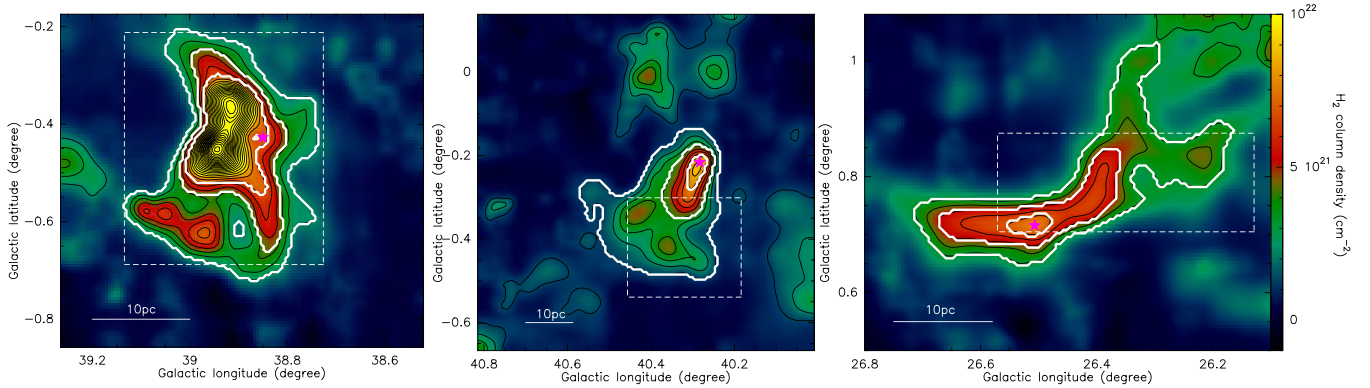


Figure 16. Colour and contours are the ^{13}CO -based H_2 column density images of three of our clouds that are in common with H09’s sample. The white dashed boxes show the area used by H09 to derive the large-scale masses represented as cyan symbols in Fig. 15.

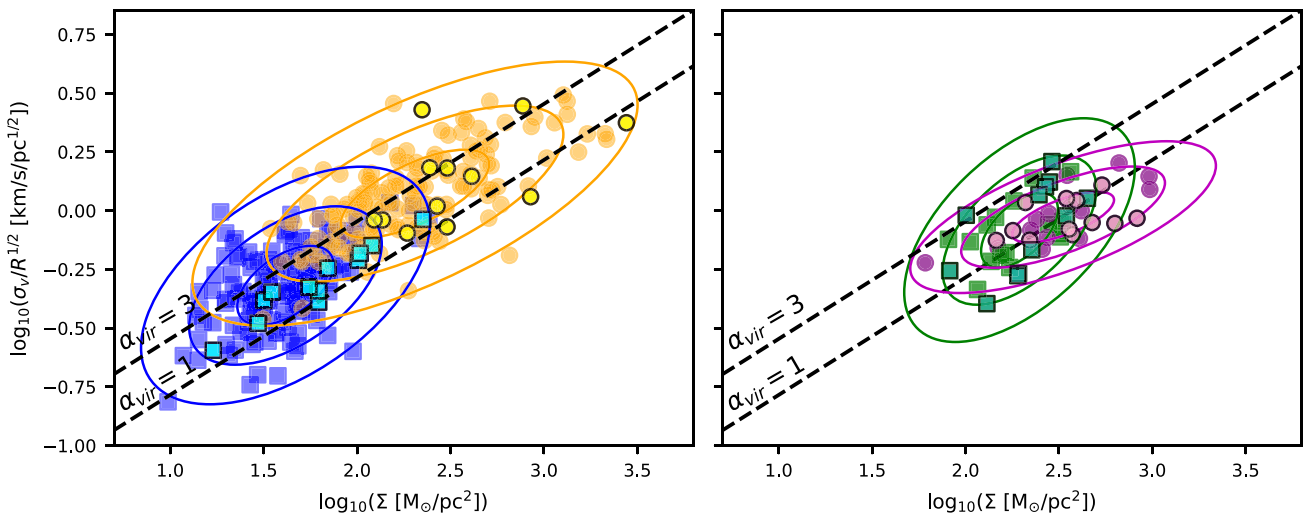


Figure 17. Heyer’s plots (left): measurements from H09 on large (blue) and small (orange) scales. The points highlighted in cyan and yellow with black edges are those clouds in common with our sample; (right): Measurements from our study on large (green) and small (magenta) scales. The clouds in common with H09’s sample are highlighted with light green and pink symbols with black edges. On each panel, the ellipses show the 1σ , 2σ , 3σ ellipses for each distributions, where σ is the standard deviation. Lines of constant virial ratios of 1 and 3 are shown as black dashed lines.

area of the plot. This is a direct consequence of the density profile of the clouds being close to $\rho \propto r^{-1}$ on those scales and velocity dispersion profiles close to $\sigma \propto r^{0.5}$. We also notice the quasi-absence of points below a $100 M_{\odot}/\text{pc}^{-2}$. As noted by Schruba, Kruijssen & Leroy (2019), molecular clouds with lower mass surface density are non-self-gravitating. As our comparison with the MD17 virial ratio distribution shows, we are here biased towards the most self-gravitating clouds of the Milky Way population, it is therefore consistent to have nearly no measurements with mass surface density below $100 M_{\odot}/\text{pc}^{-2}$.

5.3 Clump mass surface density versus β

In their study of a sample of 29 clumps, Traficante et al. (2020) found that the velocity dispersion profile index β depends on the clump mass surface density. In that study, they determined that clumps at higher mass surface density (and mass) tend to have shallower velocity dispersion profiles (i.e. lower β values) than low mass surface density clumps. The conclusion from that study was that the kinematics of high mass surface density clumps is dominated by

gravitational collapse leading to a departure from Larson’s relation, believed to be driven by turbulence.

Fig. 18 (top row) shows the velocity dispersion measurements obtained on the largest clump and cloud scales (Table 2) for each clump–cloud pair. Those measurements are obtained using the multiple Gaussian fit method. Clumps have been categorized into three groups according to their mass surface density following similar ranges as in Traficante et al. (2020). The median β values given in each panel indicates that there is no significant difference between the three groups. However, the way Traficante et al. (2020) have measured their velocity dispersion is different to what has been done here when using the Gaussian fit method. The main difference resides in the fact that they have performed a pixel-by-pixel analysis of the $^{13}\text{CO}(1-0)$ cube, by first clipping low signal-to-noise voxels, and then performing a second moment integration. As a result, the low intensity wings that we do detect, because of the spatial averaging, and fit are not represented in their velocity dispersion measurements. The closest velocity dispersion measurements we have made to those quoted in Traficante et al. (2020) are those obtained with our peak method (see Appendix B). As it can be

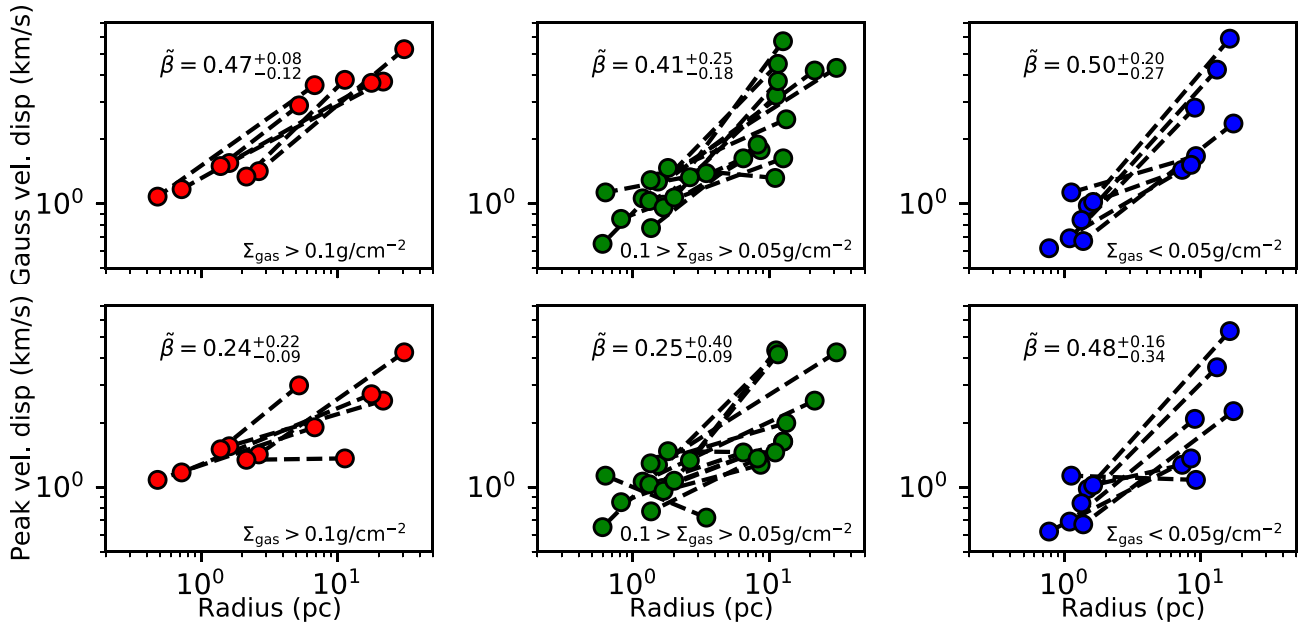


Figure 18. Velocity dispersion profiles using only the measurements obtained on the largest clump and cloud scales (i.e. those quoted in Table 2). Clumps have been categories in three groups according to their average mass surface densities, each panel corresponding to one of those groups, with the range of corresponding mass surface densities being indicated. The top row corresponds to velocity dispersion measurements obtained from Gaussian fitting, the bottom row corresponds to velocity dispersion measurements obtained using the peak method. Measurements from one clump-cloud pair are linked by a dashed black line. The median β value, i.e. $\tilde{\beta}$, and the corresponding 16th and 84th percentiles are indicated in each panel.

seen in Fig. 18 (bottom row), using those peak velocity dispersion measurement does change the picture. Now we do see, albeit small number statistics, the same trend as that observed by Traficante et al. (2020), that is the highest mass surface density clumps have shallower velocity dispersion profiles. The main reason for the change in the median β value is the decrease of the cloud-scale velocity dispersion measurements when using the peak method (see Appendix B).

This leaves us with two possible interpretations regarding the differences observed between the two rows of Fig. 18. The first one is that the high velocity wings that we fit using our multiple Gaussian fitting are unrelated to the clouds and that this method tends to overestimate the $^{13}\text{CO}(1-0)$ velocity dispersion measurements. Note, however, that this overestimation would mostly be towards high-mass surface density clumps since the low-mass ones (right-hand panels) remain mostly unchanged between the two methods. But if the high velocity wings were to be unrelated to the cloud of interest then there is no reason why one should observe a correlation between their presence and the clump mass surface density. The second interpretation is that those high-velocity wings are truly associated with the clouds, and therefore the trend observed by Traficante et al. (2020) between β and the clump mass surface density is an artefact originating from their non-detection. While, in our view, this is the most likely interpretation, the comparison between the two methods still shows an interesting result in that high-mass surface density clumps preferentially have parent clouds with highly complex kinematics. Whether complex velocity fields within molecular clouds are required for the formation of high-mass surface density clumps, or whether high-mass surface density clumps and their associated stellar feedback are responsible for generating complex velocity fields on larger scales remains to be understood.

5.4 Dynamically decoupled clumps

As the comparison of our observed profiles and spherical models have shown, the discontinuity in the observed velocity dispersion profiles is most likely the result of the combination of projection effects and a genuine change of the velocity dispersion profile index from $\beta \simeq 0.5$ on large scales to $\beta \simeq 0$ on small scales. However, one can wonder how sensitive the observed velocity dispersion profiles are to the exact value of β as the clumps only have a limited number of angular resolution elements in them. To test this, we built spherical models of varying β index in order to set some constraints on the range of values compatible with our observations. Fig. 19 displays the observed clump-scale velocity profiles along with different spherical models. Each panel corresponds to models of the same mass and radius, but with different velocity dispersion profiles. One can see that the different profiles are better resolved for the largest clouds, as expected. With this models in hands, it is also clear that $|\beta| < 0.2$ in all clumps, confirming the fact that the clump velocity dispersion profiles are flat and significantly different from Larson's profile.

The velocity dispersion discontinuity observed in Fig. 7 between the $\text{N}_2\text{H}^+(1-0)$ and the $^{13}\text{CO}(1-0)$ measurements is, according to our models, the result of foreground/background layers of low-density and high-velocity dispersion gas that contaminate the $^{13}\text{CO}(1-0)$ velocity dispersion measurements at small radii. If this interpretation of the observed profiles is correct, measuring the gas velocity dispersion with a line emission that traces intermediate gas densities should bridge, to some extent, the observed velocity dispersion discontinuity. To test this conjuncture, we used the CHIMPS $^{13}\text{CO}(3-2)$ survey data (Rigby et al. 2016). Indeed, being a higher transition line, $^{13}\text{CO}(3-2)$ is optically thinner and less extended than $^{13}\text{CO}(1-0)$, making it a good tracer of intermediate gas densities. However, only eight of our clouds have been covered by CHIMPS, amongst which one shows clear sign of self-absorption and has therefore

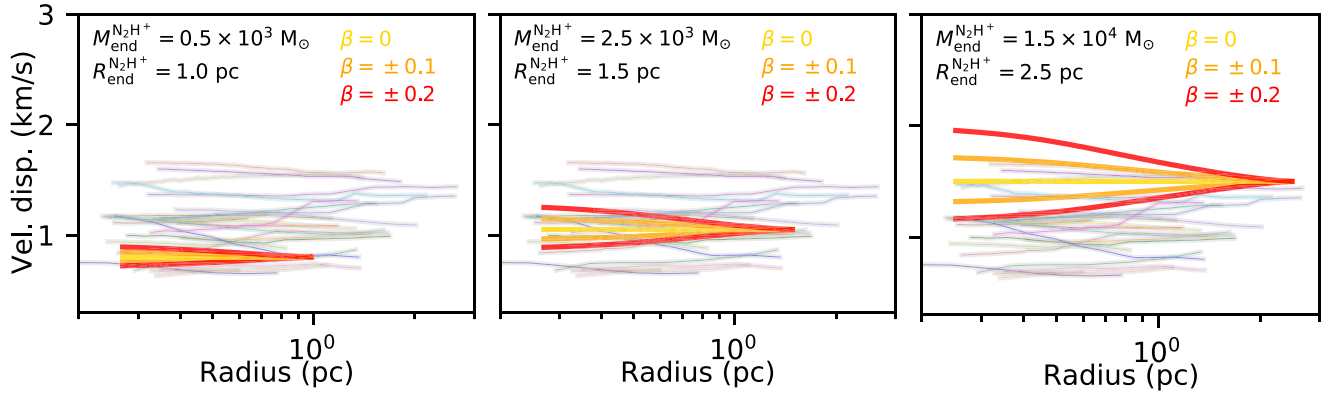


Figure 19. Velocity dispersion profiles. The models displayed in each of the three panels correspond to three different clump masses and radii, but all with the same density profile $\gamma = 2$. The yellow, orange, and red solid lines correspond to models with velocity dispersion profile index $\beta = 0$, $\beta = \pm 0.1$, and $\beta = \pm 0.2$, respectively. The observed profiles are represented with thin coloured lines.

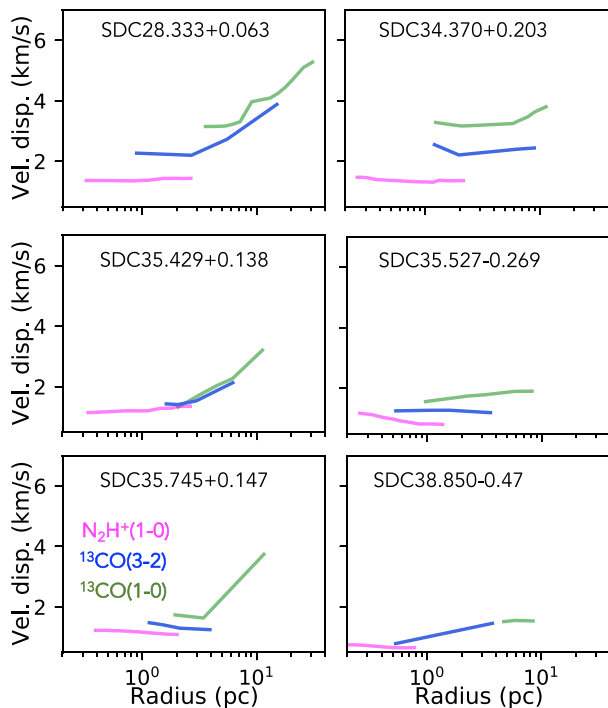


Figure 20. Velocity dispersion profiles of a subsample of 6 clouds. The magenta and green lines are the same of those plotted in Fig. 7 for those 6 clouds. The blue lines show the velocity dispersion profiles obtained from CHIMPS $^{13}\text{CO}(3-2)$ emission.

been discarded. Fig. 20 shows the velocity dispersion profiles of 6 of the 7 remaining clouds (one has been left out for a matter of figure readability). The $^{13}\text{CO}(3-2)$ line has been fitted following the exact same procedure as for the $^{13}\text{CO}(1-0)$ line. On this figure, we can see that the $^{13}\text{CO}(3-2)$ velocity dispersion systematically lies at intermediate values between that of the other two tracers. Also, in most cases, the $^{13}\text{CO}(3-2)$ profiles nicely make the bridge between the denser and more diffuse gas. Altogether, these profiles further support our interpretation that clumps are dynamically decoupled from their parent molecular clouds. A sudden change in the velocity dispersion profile of the gas has been previously observed on core-

scale, i.e. ~ 0.1 pc (e.g. Pineda et al. 2010). Whether or not this core-scale transition to coherence has the same physical origin to the proposed clump dynamical decoupling remains to be shown.

As discussed in Section 5.1, the majority of the clouds studied here are consistent with being self-gravitating on all scales. This means that the observed change in the velocity dispersion profiles is unlikely to be the result of the gas switching from a non-self-gravitating state to a self-gravitating state. When a cloud is self-gravitating, it can only be in two states: either it is collapsing, or in quasi-static equilibrium. One possibility would be for instance that the clouds from our sample, as proposed by Vázquez-Semadeni et al. (2019), are collapsing on all scales. However, the collapse in these models is scale free, with no transition regime at any scale. It is important to note though that protostellar outflows (e.g. Duarte-Cabral et al. 2012; Hsieh et al. 2023) are not included in such simulations, and could play a role in generating a change in the velocity dispersion profiles of collapsing clouds. It could also be that, as the specific angular momentum increases during the collapse, clumps become somewhat supported by rotation (e.g. Lee & Hennebelle 2016). However, this seems incompatible with a steeper clump density profile, and no systematic observation of rotation motion is observed in these clumps (Peretto et al. in preparation). A third and preferred possibility is that clouds are stable on the largest scales and that they collapse on clump scale. Indeed, both density ($\gamma = 2$) and velocity dispersion profiles ($\beta = 0$) derived from our 1D modelling of the clumps are asymptotic solutions to a spherical isothermal non-free-falling collapsing cloud with initial uniform density (Larson 1969; Penston 1969), and as noted by these authors the self-similar nature of the solution means that it may apply to any structure (i.e. protostellar core, clump, cloud). Note however that what we observe is the velocity dispersion profile and not the infall velocity profile. Even though we do expect a relationship between the two, it is not clear whether both are expected to have the exact same index. Through recent analytical models, although with different settings, both Li (2018) and Gómez, Vázquez-Semadeni & Palau (2021) show that $\gamma = 2$ naturally arises from the gravitational collapse of cores and clumps. There is also now plenty of evidence for clump collapse and clump accretion (e.g. Peretto, André & Belloche 2006; Peretto et al. 2007; Schneider et al. 2010; Peretto et al. 2013, 2014; Traficante et al. 2018; Williams et al. 2018; Barnes et al. 2019; Schwörer et al. 2019; Peretto et al. 2020; Anderson et al. 2021; Rigby et al. 2021; Bonne et al. 2022; Zhou et al. 2022; Xu et al. 2023). A possible

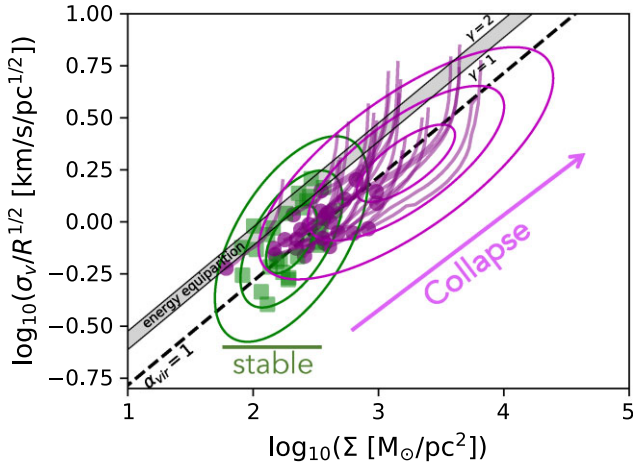


Figure 21. Same as Fig. 17 with the addition of all measurements made from $\text{N}_2\text{H}^+(1-0)$ (purple lines). The shaded area shows the region of energy equipartition for density profile indices between $\gamma = 1$ and $\gamma = 2$.

agent that might be able to stabilise the clouds on the largest scales is stellar feedback. For instance, in Watkins et al. (2019), it has been shown that stellar feedback from embedded O stars does not impact much the dynamical properties of the dense gas that has already been assembled, but does clearly modify the structure of the larger scale clouds. This is compatible with the observed change in velocity dispersion profiles presented here. Even though most clumps in our study do not have any embedded H II regions associated with them, injection of momentum and energy within the more diffuse cloud could come from nearby sites of massive star formation. A picture in which gas collapses on clump scale while being supported by turbulence on larger scales is consistent with the model proposed by Li (2017).

Another possible agent that could stabilize the cloud is magnetic field. An increasing number of studies suggest that magnetic fields are dynamically important/dominant in the low-density regions of molecular clouds. A transition in the relative orientation between magnetic field and the density gradients of interstellar structures has been interpreted as evidence for a change in the dominant energy source, from magnetic energy on large scale to gravitational energy on clump scale (e.g. Soler et al. 2013; Chen, King & Li 2016; Planck Collaboration XXXIII 2016a; Planck Collaboration XXXV 2016b; Soler et al. 2016; Tang et al. 2019; Arzoumanian et al. 2021). In Vela C, Fissel et al. (2019) determined that this change of relative orientations occur at a number density of $n \sim 10^3 \text{ cm}^{-3}$. The change in the velocity dispersion profiles we observe in our sample could then be the dynamical counterpart of that ‘magnetic’ transition. Fig. 21 shows the same plot as in Fig. 17 in which the largest cloud scale measurements and all the clump scale measurements are shown. On that plot it becomes obvious that clumps behave differently than their parent clouds. The clump mass surface densities increase over two order of magnitudes along lines of constant virial ratios except towards the most central points where β and the virial ratios increase. To our knowledge no theoretical equivalent to the plots we are producing here exists. However, a scenario in which parsec-scale clumps are collapsing while their parent molecular clouds are in quasi-static equilibrium seems to intuitively match what we see.

An important aspect of Fig. 7 is the relatively large range of velocity dispersion profile indices on cloud scale (the green lines). They range from being flat $\beta \sim 0$ to relatively steep $\beta > 0.5$. The fact that molecular clouds of several $10^4 M_\odot$ on tens of parsec-

scale may have velocity dispersions that are barely above 1 km s^{-1} clearly shows that Larson’s relation is just a statistical average over clouds of very different dynamical states. In fact, it is possible that the range of velocity dispersion profiles correspond to different evolutionary stages in the formation and evolution of molecular clouds and clumps within. Any scenario that attempt to explain the dynamical decoupling of clumps needs to do so in the context of this observed variety of large-scale velocity dispersion profiles.

6 SUMMARY AND CONCLUSION

We performed the analysis of 27 IRDC embedded within 24 molecular clouds. We computed the mass, velocity dispersion, and virial ratio profiles of each of them using three different data sets: *Herschel*-derived H_2 column density maps, GRS $^{13}\text{CO}(1-0)$ -derived H_2 column density cubes, and $\text{N}_2\text{H}^+(1-0)$ data cubes. The combination of these data allowed us to probe both the dense and diffuse parts of the clouds, with radii from $\sim 0.2 \text{ pc}$ up to $\sim 30 \text{ pc}$. Using 1D power-law models we can explain the origin of the different features observed in those profiles and we conclude that (1) the vast majority of cluster-forming molecular clouds are consistent with being self-gravitating on all scales; (2) the diffuse part of the cloud has a shallow density profile ($\gamma \sim 1$) that steepens ($\gamma \sim 2$) in the densest parts on a couple of parsec scale; (3) the velocity dispersion profile switches, for most clouds, from $\beta \sim 0.5$ in the diffuse part of the clouds to $\beta \sim 0$ in the denser parts. We discuss the possible interpretation of such a decoupling of the clumps from their surrounding cloud and conclude that the observations are best explained by a universal global collapse of dense clumps embedded within stable molecular clouds, even though we cannot completely rule out a scenario in which the entire cloud collapses, with small-scale feedback, such as protostellar outflows, impacting the gas kinematics on clump scales. We also notice that the velocity dispersion profiles on molecular cloud scales (i.e. $> 2 \text{ pc}$) show a large variety of β values, some very far from the standard Larson’s relation, which might be linked to their evolution since the time of their formation.

Understanding the origin of the observed low star formation efficiency (SFE) in molecular clouds is one of the main goals of star formation research. A low SFE involves a scale/density-dependent dynamical state of the gas in which most of a cloud mass is not directly involved in the formation of stars. Observationally, the existence of a star formation threshold has been discussed in the context of the study of nearby star-forming clouds (e.g. Heiderman et al. 2010; Lada, Lombardi & Alves 2010; Pokhrel et al. 2020). However, so far, no studies has searched for direct evidence of a transition regime in the dynamical properties of the gas within individual molecular clouds. The work presented here clearly suggests that such transition regime does exist. Because parsec-scale clumps are believed to be the direct progenitors of star clusters (e.g. Krumholz, McKee & Bland-Hawthorn 2019), our results hence suggest that star cluster formation is not a scale-free process.

Our results also carry a number of key questions and implications. First, we here do not explain what the trigger of the clump collapse is, whether it is the result of a gravitationally instability or the diffusion of magnetic fields, or any other mechanism. We also do not explain what is the main agent that counter-balance gravity in the diffuse parts of the clouds. These questions will have to be answered if one wants to derive a comprehensive scenario for the formation of star clusters. Also, one implication of our results is the fact that star formation is likely to be mostly confined to these parsec-scale collapsing clumps. Therefore their properties define the initial conditions for

cluster formation, and understanding the link, on one side, between the properties of clumps and that of their associated protostellar population, and on the other side, between the global population of Galactic clumps and the star formation rate and efficiency of the Milky Way remains a fundamental challenge.

ACKNOWLEDGEMENTS

We would like to thank the referee, Erik Rosolowsky, for a careful and well balanced report that helped improving the quality of the paper. NP and AJR acknowledges the support of STFC consolidated grant number ST/N000706/1 and ST/S00033X/1. FL acknowledges support by the Marie Curie Action of the European Union (project *MagiKStar*, Grant agreement number 841276). GAF acknowledges support from the Collaborative Research Centre 956, funded by the Deutsche Forschungsgemeinschaft (DFG) project ID 184018867. GAF also acknowledges support from the University of Cologne and its Global Faculty Program. This work is based on observations carried out under project number 023–13 with the IRAM 30 m telescope. IRAM is supported by INSU/CNRS (France), MPG (Germany), and IGN (Spain).

DATA AVAILABILITY

The *Herschel* and GRS data used in this article are already publicly available on their respective survey webpages. The IRAM 30m $N_2H^+(1-0)$ data can be provided upon reasonable request to N. Peretto.

REFERENCES

- Anderson M. et al., 2021, *MNRAS*, 508, 2964
 Arzoumanian D. et al., 2021, *A&A*, 647, A78
 Ballesteros-Paredes J., Hartmann L. W., Vázquez-Semadeni E., Heitsch F., Zamora-Avilés M. A., 2011, *MNRAS*, 411, 65
 Barnes P. J., Müller E., Indermuehle B., O’Dougherty S. N., Lowe V., Cunningham M., Hernandez A. K., Fuller G. A., 2015, *ApJ*, 812, 6
 Barnes A. T. et al., 2019, *MNRAS*, 486, 283
 Barnes A. T. et al., 2021, *MNRAS*, 503, 4601
 Battersby C. et al., 2011, *A&A*, 535, A128
 Bernard J.-P. et al., 2010, *A&A*, 518, L88+
 Bertoldi F., McKee C. F., 1992, *ApJ*, 395, 140
 Bisbas T. G., Tanaka K. E. I., Tan J. C., Wu B., Nakamura F., 2017, *ApJ*, 850, 23
 Blake G. A., Sutton E. C., Masson C. R., Phillips T. G., 1987, *ApJ*, 315, 621
 Bonne L., Peretto N., Duarte-Cabral A., Schmiedeke A., Schneider N., Bontemps S., Whitworth A., 2022, *A&A*, 665, A22
 Bonnell I. A., Bate M. R., 2006, *MNRAS*, 370, 488
 Chen C.-Y., King P. K., Li Z.-Y., 2016, *ApJ*, 829, 84
 Clemens D. P., Sanders D. B., Scoville N. Z., Solomon P. M., 1986, *ApJS*, 60, 297
 Dale J. E., Ercolano B., Bonnell I. A., 2012, *MNRAS*, 424, 377
 Dewangan L. K., Ojha D. K., Zinchenko I., Baug T., 2018, *ApJ*, 861, 19
 Dib S., Kim J., Vázquez-Semadeni E., Burkert A., Shadmehri M., 2007, *ApJ*, 661, 262
 Dobbs C. L., Burkert A., Pringle J. E., 2011, *MNRAS*, 413, 2935
 Duarte-Cabral A., Chrysostomou A., Peretto N., Fuller G. A., Matthews B., Schieven G., Davis G. R., 2012, *A&A*, 543, A140
 Duarte-Cabral A. et al., 2021, *MNRAS*, 500, 3027
 Ellsworth-Bowers T. P. et al., 2013, *ApJ*, 770, 39
 Fissel L. M. et al., 2019, *ApJ*, 878, 110
 Gómez G. C., Vázquez-Semadeni E., Palau A., 2021, *MNRAS*, 502, 4963
 Goodman A. A., Rosolowsky E. W., Borkin M. A., Foster J. B., Halle M., Kauffmann J., Pineda J. E., 2009, *Nature*, 457, 63
 Griffin M. J. et al., 2010, *A&A*, 518, L3+
 Grudić M. Y., Guszejnov D., Offner S. S. R., Rosen A. L., Raju A. N., Faucher-Giguère C.-A., Hopkins P. F., 2022, *MNRAS*, 512, 216
 Hacar A., Alves J., Burkert A., Goldsmith P., 2016, *A&A*, 591, A104
 Hacar A., Tafalla M., Forbrich J., Alves J., Meingast S., Grossschedl J., Teixeira P. S., 2018, *A&A*, 610, A77
 Hartmann L., Burkert A., 2007, *ApJ*, 654, 988
 Haworth T. J. et al., 2015, *MNRAS*, 450, 10
 Heiderman A., Evans N. J. II, Allen L. E., Huard T., Heyer M., 2010, *ApJ*, 723, 1019
 Hennebelle P., Chabrier G., 2008, *ApJ*, 684, 395
 Henshaw J. D., Caselli P., Fontani F., Jiménez-Serra I., Tan J. C., 2014, *MNRAS*, 440, 2860
 Hernandez A. K., Tan J. C., 2015, *ApJ*, 809, 154
 Heyer M., Krawczyk C., Duval J., Jackson J. M., 2009, *ApJ*, 699, 1092
 Hildebrand R. H., 1983, *QJRAS*, 24, 267
 Hopkins P. F., 2012, *MNRAS*, 423, 2037
 Hsieh C.-H. et al., 2023, *ApJ*, 947, 25
 Jackson J. M. et al., 2006, *ApJS*, 163, 145
 Kauffmann J., Pillai T., Shetty R., Myers P. C., Goodman A. A., 2010, *ApJ*, 716, 433
 Kauffmann J., Pillai T., Goldsmith P. F., 2013, *ApJ*, 779, 185
 Kim J.-G., Kim W.-T., Ostriker E. C., 2018, *ApJ*, 859, 68
 Krumholz M. R., McKee C. F., 2005, *ApJ*, 630, 250
 Krumholz M. R., Tan J. C., 2007, *ApJ*, 654, 304
 Krumholz M. R., McKee C. F., Bland-Hawthorn J., 2019, *ARA&A*, 57, 227
 Kutner M. L., Ulich B. L., 1981, *ApJ*, 250, 341
 Lada C. J., Lombardi M., Alves J. F., 2010, *ApJ*, 724, 687
 Langer W. D., Penzias A. A., 1990, *ApJ*, 357, 477
 Larson R. B., 1969, *MNRAS*, 145, 271
 Larson R. B., 1981, *MNRAS*, 194, 809
 Lee Y.-N., Hennebelle P., 2016, *A&A*, 591, A30
 Li G.-X., 2017, *MNRAS*, 465, 667
 Li G.-X., 2018, *MNRAS*, 477, 4951
 Li G.-X., Wyrowski F., Menten K., Megeath T., Shi X., 2015, *A&A*, 578, A97
 Marsh K. A., Whitworth A. P., Lomax O., 2015, *MNRAS*, 454, 4282
 Miville-Deschênes M.-A., Murray N., Lee E. J., 2017, *ApJ*, 834, 57 (MD17)
 Molinari S. et al., 2010, *A&A*, 518, L100+
 Motte F., André P., 2001, *A&A*, 365, 440
 Nakamura F., Li Z.-Y., 2007, *ApJ*, 662, 395
 Offner S. S. R., Liu Y., 2018, *Nat. Astron.*, 2, 896
 Ott S., 2010, in Mizumoto Y., Morita K. I., Ohishi M., eds, ASP Conf. Ser. Vol. 434, *Astronomical Data Analysis Software and Systems XIX*. Astron. Soc. Pac., San Francisco, p. 139
 Padoan P., Nordlund A., Jones B. J. T., 1997, *MNRAS*, 288, 145
 Padoan P., Pan L., Juvella M., Haugbølle T., Nordlund Å., 2020, *ApJ*, 900, 82
 Palau A. et al., 2014, *ApJ*, 785, 42
 Penston M. V., 1969, *MNRAS*, 144, 425
 Peretto N., Fuller G. A., 2009, *A&A*, 505, 405
 Peretto N., André P., Belloche A., 2006, *A&A*, 445, 979
 Peretto N., Hennebelle P., André P., 2007, *A&A*, 464, 983
 Peretto N. et al., 2010, *A&A*, 518, L98+
 Peretto N. et al., 2013, *A&A*, 555, A112
 Peretto N. et al., 2014, *A&A*, 561, A83
 Peretto N., Lenfestey C., Fuller G. A., Traficante A., Molinari S., Thompson M. A., Ward-Thompson D., 2016, *A&A*, 590, A72 (P16)
 Peretto N. et al., 2020, *MNRAS*, 496, 3482
 Piazzo L., Calzoletti L., Faustini F., Pestalozzi M., Pezzuto S., Elia D., di Giorgio A., Molinari S., 2015, *MNRAS*, 447, 1471
 Pilbratt G. L. et al., 2010, *A&A*, 518, L1+
 Pineda J. E., Goodman A. A., Arce H. G., Caselli P., Foster J. B., Myers P. C., Rosolowsky E. W., 2010, *ApJ*, 712, L116
 Planck Collaboration XXV, 2011, *A&A*, 536, A25
 Planck Collaboration XXXIII, 2016a, *A&A*, 586, A136
 Planck Collaboration XXXV, 2016b, *A&A*, 586, A138
 Poglitsch A. et al., 2010, *A&A*, 518, L2+
 Pokhrel R. et al., 2020, *ApJ*, 896, 60

- Reid M. J. et al., 2009, *ApJ*, 700, 137
 Rigby A. J. et al., 2016, *MNRAS*, 456, 2885
 Rigby A. J. et al., 2018, *A&A*, 615, A18
 Rigby A. J. et al., 2019, *A&A*, 632, A58
 Rigby A. J. et al., 2021, *MNRAS*, 502, 4576
 Robitaille T. P., Whitney B. A., 2010, *ApJ*, 710, L11
 Roman-Duval J., Jackson J. M., Heyer M., Rathborne J., Simon R., 2010, *ApJ*, 723, 492
 Rosolowsky E. W., Pineda J. E., Kauffmann J., Goodman A. A., 2008, *ApJ*, 679, 1338
 Sadavoy S. I., Stutz A. M., Schnee S., Mason B. S., Di Francesco J., Friesen R. K., 2016, *A&A*, 588, A30
 Sanders D. B., Clemens D. P., Scoville N. Z., Solomon P. M., 1986, *ApJS*, 60, 1
 Schneider N., Csengeri T., Bontemps S., Motte F., Simon R., Hennebelle P., Federrath C., Klessen R., 2010, *A&A*, 520, A49
 Schruha A., Kruijssen J. M. D., Leroy A. K., 2019, *ApJ*, 883, 2
 Schuller F. et al., 2017, *A&A*, 601, A124
 Schwörer A. et al., 2019, *A&A*, 628, A6
 Singh A. et al., 2021, *ApJ*, 922, 87
 Smith R. J., Longmore S., Bonnell I., 2009, *MNRAS*, 400, 1775
 Soler J. D., Hennebelle P., Martin P. G., Miville-Deschênes M. A., Netterfield C. B., Fissel L. M., 2013, *ApJ*, 774, 128
 Soler J. D. et al., 2016, *A&A*, 596, A93
 Solomon P. M., Rivolo A. R., Barrett J., Yahil A., 1987, *ApJ*, 319, 730
 Tang Y.-W., Koch P. M., Peretto N., Novak G., Duarte-Cabral A., Chapman N. L., Hsieh P.-Y., Yen H.-W., 2019, *ApJ*, 878, 10
 Traficante A. et al., 2011, *MNRAS*, 416, 2932
 Traficante A., Fuller G. A., Smith R. J., Billot N., Duarte-Cabral A., Peretto N., Molinari S., Pineda J. E., 2018, *MNRAS*, 473, 4975
 Traficante A., Fuller G. A., Duarte-Cabral A., Elia D., Heyer M. H., Molinari S., Peretto N., Schisano E., 2020, *MNRAS*, 491, 4310
 Vázquez-Semadeni E., González-Samaniego A., Colín P., 2017, *MNRAS*, 467, 1313
 Vázquez-Semadeni E., Palau A., Ballesteros-Paredes J., Gómez G. C., Zamora-Avilés M., 2019, *MNRAS*, 490, 3061
 Wang P., Li Z.-Y., Abel T., Nakamura F., 2010, *ApJ*, 709, 27
 Watkins E. J., Peretto N., Marsh K., Fuller G. A., 2019, *A&A*, 628, A21
 Weis M., Walch S., Seifried D., Ganguly S., 2022, preprint (arXiv:2208.11705)
 Williams G. M., Peretto N., Avison A., Duarte-Cabral A., Fuller G. A., 2018, *A&A*, 613, A11
 Wong T. et al., 2019, *ApJ*, 885, 50
 Xu F.-W. et al., 2023, *MNRAS*, 520, 3259
 Ysard N., Köhler M., Jones A., Miville-Deschênes M. A., Abergel A., Fanciullo L., 2015, *A&A*, 577, A110
 Yuan Y., Krumholz M. R., Burkhardt B., 2020, *MNRAS*, 498, 2440
 Zhou J.-W. et al., 2022, *MNRAS*, 514, 6038
 Zuckerman B., Evans N. J. II, 1974, *ApJ*, 192, L149

SUPPORTING INFORMATION

Supplementary data are available at [MNRAS](https://academic.oup.com/mnras/article/525/2/2935/7246075) online.

Appendix A. Summary figures.

Please note: Oxford University Press is not responsible for the content or functionality of any supporting materials supplied by the authors. Any queries (other than missing material) should be directed to the corresponding author for the article.

APPENDIX A: SUMMARY FIGURES

This appendix is supplied as online supplementary material.

APPENDIX B: VELOCITY DISPERSION: METHOD COMPARISON

In addition to the Gaussian fits presented in the paper, we also tested two other methods that are often used in the literature. The first of those is a traditional moment method, referred to as moments in this appendix, for which we compute the zeroth-, first-, and second-order moments within a given velocity interval. The zeroth-order moment is used to compute the mass. The first- and second-order moments are used to compute the velocity dispersion. The velocity intervals are determined by eye and are defined so that the cloud main component and any overlapping emission from overlapping clouds, in velocity space, are included (see Fig. B1 for an example). The second method we tested, referred to as peak in this Appendix, is based on the FWHM of the column density spectrum peak. The velocity dispersion is taken as FWHM/2.35, and the velocity interval over which the mass is calculated is taken as eight times the dispersion, and is centred in a way that matches the asymmetry of the peak velocity with respect to the FWHM velocity interval (see Fig. B1). To obtain the mass we just integrate the spectra over that velocity range.

Fig. B2 compares the resulting masses, velocity dispersions, and virial ratios as obtained for the three methods (Gaussian fit, moment, and peak). The top row shows the comparison between the Gaussian fit and peak methods, while the bottom row shows the comparison between the Gaussian fit and the moment method. This shows that, as far as the masses are concerned, the method used does not make much of a difference, and the reason is that most of the mass is located within the central few channels that are covered by all three methods. The main differences between the methods are related to the estimate of the velocity dispersions. One can see that the peak method nearly systematically produces lower velocity dispersions

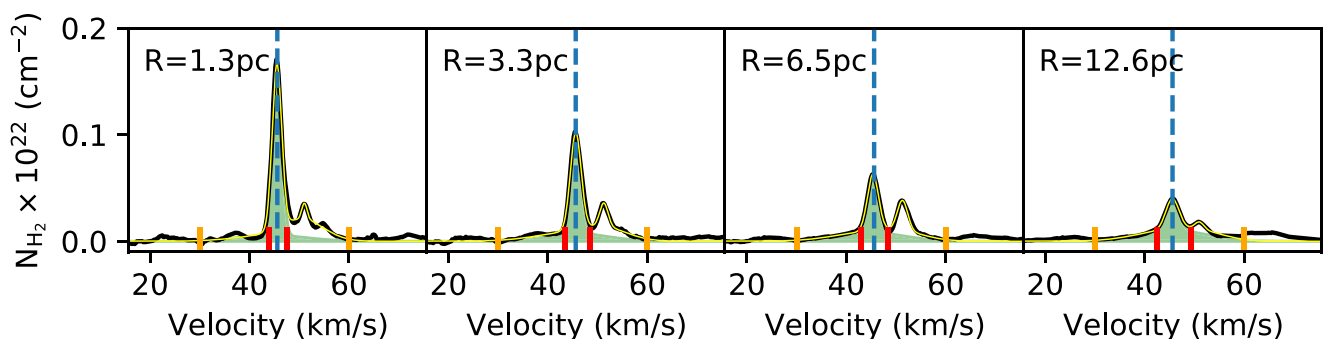


Figure B1. Examples of ^{13}CO -based H_2 column density spectra for SDC18.624–0.070 in black. The multi-Gaussian fits are shown as thin yellow lines, the shaded green area corresponds to the components we believe are associated with the cloud. The velocity intervals for the Moment method are shown as vertical orange ticks, while the velocity intervals for the peak method are shown as vertical red ticks.

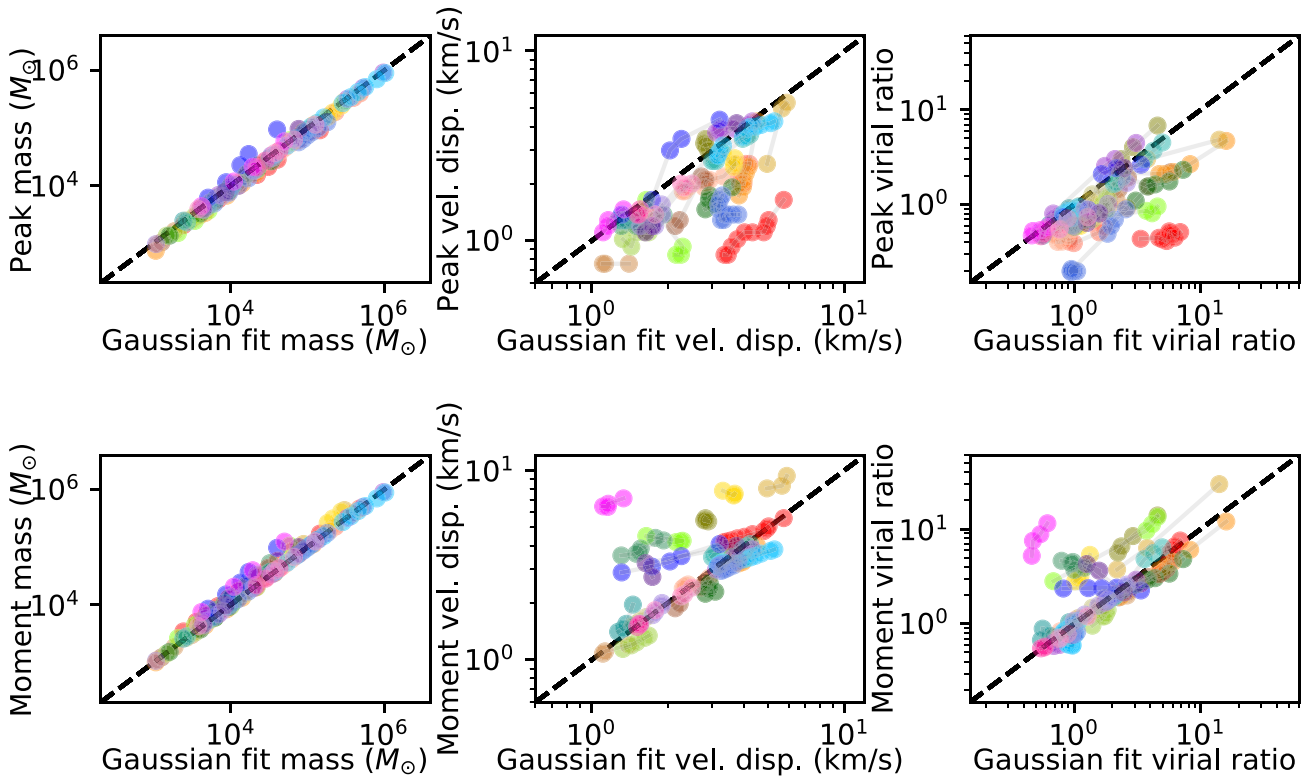


Figure B2. Comparing cloud properties using different methods for estimating the velocity dispersion of $^{13}\text{CO}(1-0)$. In the top row we compare the Gaussian fit results on the x -axis, the method used in the rest of the paper, against the peak results on the y -axis. In the bottom row, the x -axes remain the same, but the y -axis shows the moment results. The black dashed lines represent the one-to-one relationships, and each colour corresponds to a different cloud, each cloud having a number of measurements taken at different radii.

than the Gaussian fit method. This is expected as that method only focusses on the central peak of emission and will therefore exclude any large velocity dispersion wings that might be present. The results of the peak method are similar to what we would get by fitting the spectra with single Gaussians. When comparing the moments results to those of the Gaussian fits one can see that they are, overall, in broader agreement, even though the moment method tend to produce larger velocity dispersions for some clouds. Those are the clouds for which a spectrally overlapping components has been excluded from our Gaussian fit results but included within the moment one (as for SDC18.624–0.070 presented in Fig. B1). The virial ratios differences are a direct consequences of the differences observed in the velocity dispersion measurements, leading to virial ratios that can be as high as ~ 50 in some cases when using the moment method and as low as ~ 0.1 when using the peak method.

For completeness, we also plot the mass, velocity dispersion, and virial profiles as obtained for both the moment and peak methods (see Fig. B3). As expected from our previous discussion, the main differences lie in the velocity dispersion profiles, whereby the moment method produce a larger discontinuity between clump and cloud scales, while the peak method makes the discontinuity less prominent. However, as our models show (Figs 9 and 10) for shallow cloud density profiles as those observed (i.e. $\gamma \leq 1.5$) significant velocity discontinuities are expected, which indicates that the peak method is likely underestimating the true gas velocity dispersion.

Overall, we believe that the Gaussian fits method provide better results than any of the other two as it allows to include large velocity dispersion wings and exclude, at the same time, components that we know are not physically related to the cloud of interest. It is definitely the best method to measure the velocity dispersion of ^{13}CO clouds.

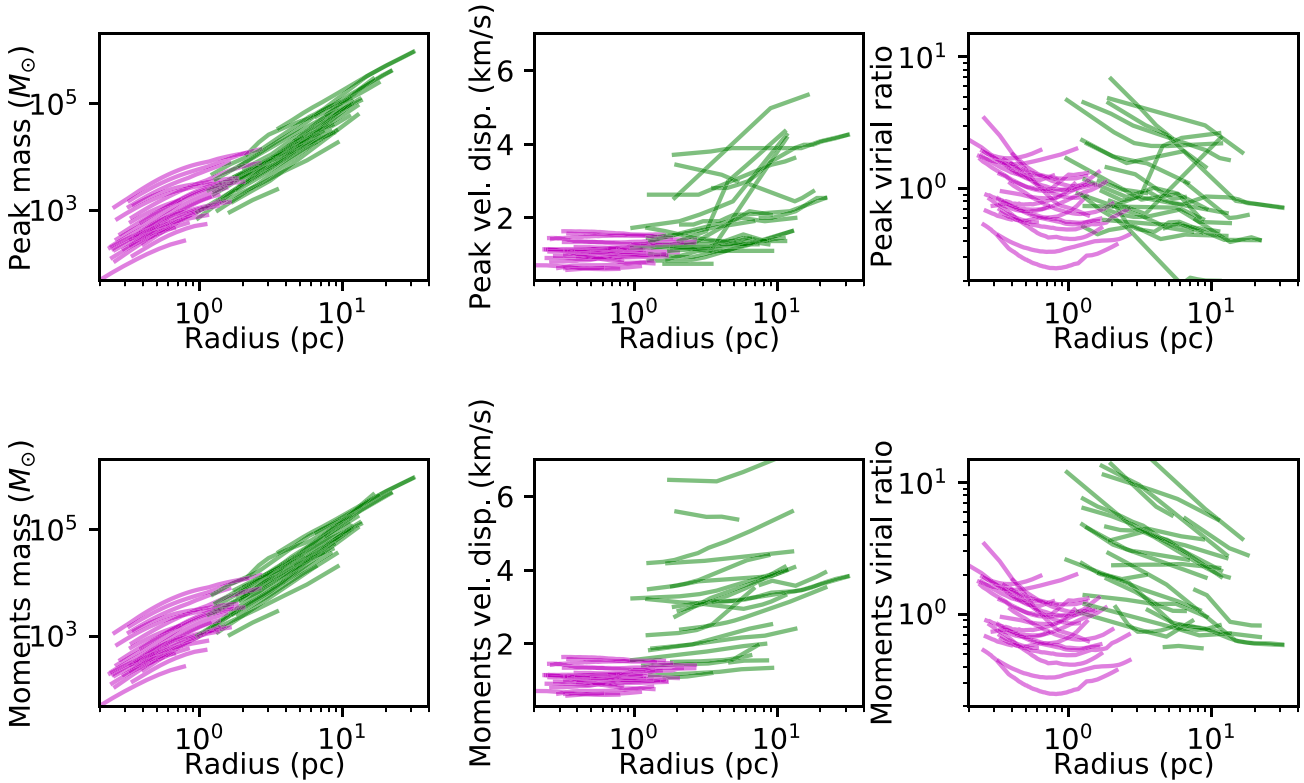


Figure B3. Same as Fig. 7 but with the mass and velocity dispersion estimated via the peak (top) and moment (bottom) methods.

APPENDIX C: THE $N_{\text{N}_2\text{H}^+}^{\text{edge}} = 0$ CASE

In this Appendix, we quantify the impact of not removing a background column density on the clump-scale mass profile, effectively setting $N_{\text{N}_2\text{H}^+}^{\text{edge}} = 0$. Fig. C1 shows the corresponding mass profiles. One can see that the profiles, as expected, appear a lot more continuous than when a background is removed. Interestingly, there

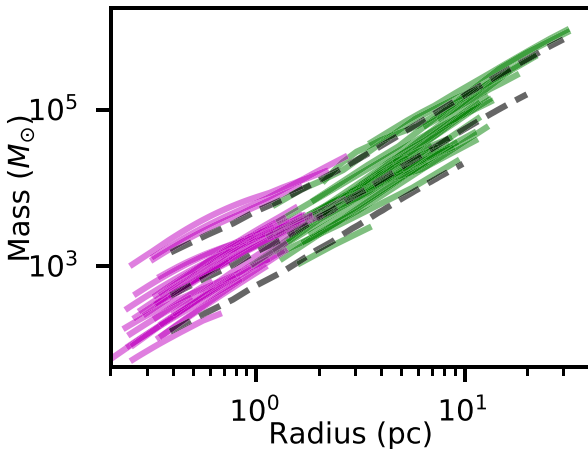


Figure C1. Same as the mass profiles displayed in Fig. 7 but for the case where $N_{\text{N}_2\text{H}^+}^{\text{edge}} = 0$ (i.e. no background subtraction for the clump-scale masses). The three black dashed lines show three $\gamma_{\text{in}} = 2$ and $\gamma_{\text{out}} = 1$ models of three different masses and external radii. These models are not convolved in order to maximise the visibility of the slope change.

is no obvious change of mass profile slope, which seems to be in apparent contradiction with our previous claim that clumps have a steeper density profile than their parent molecular cloud. In order to check whether or not we would be able to observe such a slope change, we produced a series of three models (see Section 4) with $\gamma_{\text{in}} = 2$ and $\gamma_{\text{out}} = 1$ of different masses. Those three models are represented as black dashed lines in Fig. C1. These models clearly show that as a result of line-of-sight mass contamination one is unable to observe any significant change in the mass profile slope, i.e. the measured mass at clump scale is dominated by the cloud-scale foreground/background mass (see also Fig. 11). Therefore, the apparent contradiction is not one, and background subtraction is necessary if one wants to evidence any change in the radial density profile power-law index.

APPENDIX D: MODELS OF BIJECTIVE MASS AND VELOCITY DISPERSION ESTIMATES

Here, we describe how we built the projected version of the spherical models presented in the paper.

First, let us consider a sphere of radius with the following the following density profile:

$$\rho(r) = \rho_0 \left(\frac{r}{r_0} \right)^{-\gamma}, \quad (\text{D1})$$

where r_0 and ρ_0 are normalization constants. Then the enclosed mass within radius r , $m_{\text{real}}(r)$, is given by

$$m_{\text{real}}(r) = \int_0^r \rho_0 \left(\frac{r}{r_0} \right)^{-\gamma} 4\pi r^2 dr, \quad (\text{D2})$$

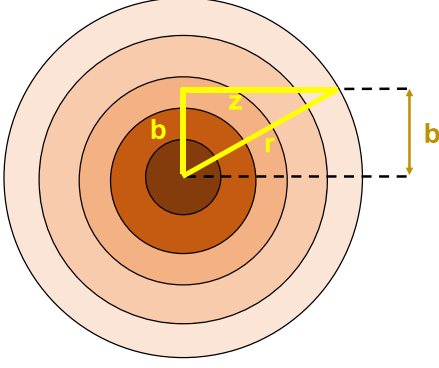


Figure D1. Sketch illustrating the definition of the different variables.

$$m_{\text{real}}(r) = 4\pi\rho_0 r_0^\gamma \frac{r^{3-\gamma}}{3-\gamma}. \quad (\text{D3})$$

Now we need to derive the observed mass, $m_{\text{obs}}(r)$, derived from the observed column density map using the bijection method. The column density is obtained by

$$N(b) = 2 \int_0^{z_{\text{max}}} \rho(z) dz, \quad (\text{D4})$$

where b is the impact parameter, equivalent to the projected radius, z is the distance along the line of sight from the tangent point of the sphere of radius b , and z_{max} is the maximum distance along the line of sight from the tangent point to the edge of the cloud. Fig. D1 summarizes these different variables. The variable z can be expressed as

$$z = \sqrt{r^2 - b^2}, \quad (\text{D5})$$

with its maximum value z_{max} being

$$z_{\text{max}} = \sqrt{R_{\text{cloud}}^2 - b^2}, \quad (\text{D6})$$

where R_{cloud} is the cloud radius. Equation (D4) can then be written as

$$N(b) = 2\rho_0 r_0^\gamma \int_0^{z_{\text{max}}} (b^2 + z^2)^{-\gamma/2} dz. \quad (\text{D7})$$

The observed mass within a projected radius $b = r$ is given by

$$m_{\text{obs}}(r) = 2\pi \int_0^r N(b) b db. \quad (\text{D8})$$

Equation (D7) can be solved analytically for some specific values of γ , but can easily be solved numerically for any value of γ as long as $0 \leq \gamma < 3$.

Now, let us consider that the same sphere has the following velocity dispersion profile:

$$\sigma(r) = \sigma_0 \left(\frac{r}{r_0} \right)^\beta, \quad (\text{D9})$$

where σ_0 is a normalization constant. The corresponding mass-weighted velocity dispersion is given by

$$\bar{\sigma}_{\text{real}}(r) = \frac{\int_0^r \sigma(r) \rho(r) 4\pi r^2 dr}{m_{\text{real}}(r)}, \quad (\text{D10})$$

$$\bar{\sigma}_{\text{real}}(r) = \frac{4\pi\sigma_0\rho_0 r_0^{\gamma-\beta}}{m_{\text{real}}(r)} \frac{r^{3-\gamma+\beta}}{3-\gamma+\beta}. \quad (\text{D11})$$

Now, the observed velocity dispersion $\bar{\sigma}_{\text{obs}}$ is given by

$$\bar{\sigma}_{\text{obs}}(b) = \frac{\int_0^{z_{\text{max}}} \rho(z) \sigma(z) dz}{N(b)}, \quad (\text{D12})$$

$$\bar{\sigma}_{\text{obs}}(b) = \rho_0 \sigma_0 r_0^{\gamma-\beta} \frac{\int_0^{z_{\text{max}}} (b^2 + z^2)^{(\beta-\gamma)/2} dz}{N(b)}. \quad (\text{D13})$$

Equation (D13) can easily be numerically integrated for different combinations of β and γ values. Note that here, we derived the expression of $\bar{\sigma}_{\text{obs}}(r)$ and $m_{\text{obs}}(r)$ in the case of single power law profiles, but, when extended to broken power laws, the expressions becomes longer as one integration has to be made for each part of the profile. The logic behind it being the same as for single power-law profiles, we will not derive their expressions here.

APPENDIX E: IMPACT OF NON-UNIFORM VELOCITY DISPERSION PROFILES ON THE VIRIAL RATIO PARAMETER

As noted by MD17 the non-uniformity of the velocity dispersion within clouds impact their virial ratio estimates. Here, we show the derivation of the corresponding correcting factor, noted a_3 in MD17.

The kinetic energy of a spherical cloud of radius R , density profile $\rho = \rho(R) \left(\frac{r}{R} \right)^{-\gamma}$, and velocity dispersion profile $\sigma(r) = \sigma(R) \left(\frac{r}{R} \right)^\beta$ is given by

$$E_k(r) = \frac{3}{2} \int_0^r \rho(r) \sigma(r)^2 4\pi r^2 dr, \quad (\text{E1})$$

$$E_k(r) = 6\pi \frac{\rho(R) \sigma(R)^2 R^{\gamma-2\beta}}{3+2\beta-\gamma} r^{3+2\beta-\gamma}. \quad (\text{E2})$$

Note that here we chose $r_0 = R$ as it will simplify the calculations. In equation (E2), $\rho(R)$ and $\sigma(R)$, the density and velocity dispersion at radius $r = R$, are not observable quantities. But $\bar{\rho}(R)$ and $\bar{\sigma}(R)$ are the average density and mass-weighted velocity dispersion within radius $r = R$. One therefore needs to derive the relation between $\rho(R)$, $\sigma(R)$ and $\bar{\rho}(R)$, $\bar{\sigma}(R)$ in order to sub-in the former within the equation of kinetic energy. For the density, we have

$$\bar{\rho}(R) = \frac{\int_0^R \rho(r) 4\pi r^2 dr}{\int_0^R 4\pi r^2 dr}, \quad (\text{E3})$$

$$\bar{\rho}(R) = \rho(R) \frac{3}{3-\gamma}. \quad (\text{E4})$$

For the velocity dispersion, we have

$$\bar{\sigma}(R) = \frac{\int_0^R \sigma(r) \rho(r) 4\pi r^2 dr}{\int_0^R \rho(r) 4\pi r^2 dr}, \quad (\text{E5})$$

$$\bar{\sigma}(R) = \sigma(R) \frac{3-\gamma}{3+\beta-\gamma}. \quad (\text{E6})$$

We can now sub these expressions in the equation of kinetic energy for $r = R$:

$$E_k(R) = 2\pi \bar{\rho}(R) \bar{\sigma}(R)^2 R^3 \frac{(3+\beta-\gamma)^2}{(3-\gamma)(3+2\beta-\gamma)}, \quad (\text{E7})$$

$$E_k(R) = \frac{3}{2} M \bar{\sigma}(R)^2 \frac{(3+\beta-\gamma)^2}{(3-\gamma)(3+2\beta-\gamma)}. \quad (\text{E8})$$

The correction factor on the kinetic energy a_3 (keeping the same notation as in MD17) resulting from the non-uniform velocity dispersion is therefore given by

$$a_3 = \frac{(3+\beta-\gamma)^2}{(3-\gamma)(3+2\beta-\gamma)}. \quad (\text{E9})$$

For $\beta = 0.5$ and $\gamma = 1$, we obtain a correction factor $a_3 = \frac{25}{24}$, which is basically negligible. This is quite different to the correction

factor evaluated by MD17, which gives $a_3 = \frac{2}{3}$ for the same power-law indices. After exchanging with the authors, it has been found that MD17 wrongly assumed that the observationally measured velocity dispersion was $\sigma(R)$ as opposed to $\bar{\sigma}(R)$. This mistake leads to the differences in the estimated correction factors highlighted here. Since a_3 is close to unity, we did not take it into account in the virial ratio estimated presented in this article.

APPENDIX F: PROPERTIES COMPARISON WITH H09

In Fig. F1, we present the comparison of kinematics distances between this paper and Heyer et al. (2009). One can see that for half the clouds we have in common with H09, the distance differ. The reason is that we opted for the near kinematic distances for all of our clouds, while they opted for the far kinematic distance for

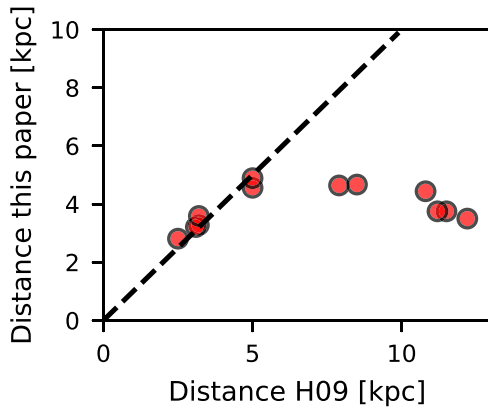


Figure F1. Distance comparison for the subsample of 12 clouds common to our study, i.e. y -axis, and that of Heyer et al. (2009), i.e. x -axis.

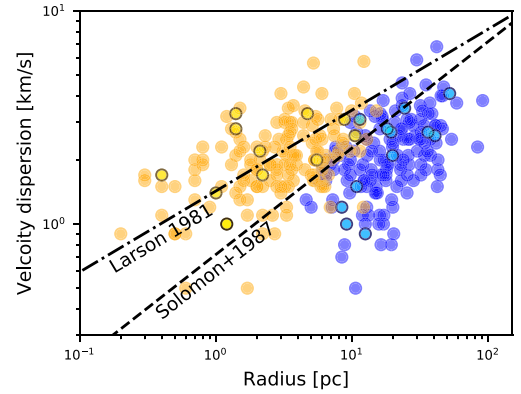


Figure F2. Radius versus velocity dispersion for all Heyer et al. (2009) measurements. The blue symbols show the measurements done within the original boxes from Solomon et al. (1987). The yellow symbols show the measurements made within the half-power isophot of the column density peak within that box. The 12 clouds that are in common between our and Heyer’s study are shown as yellow and cyan symbols. The dashed and dot-dashed lines show the Larson’s and Solomon’s relations.

a significant fraction of their sample. However, as justified in the main body of this paper, it is more likely that all this IRDC-hosting molecular clouds lie at the near distance.

In Fig. F2, we present all velocity dispersion measurements as a function of radius from H09. As explained in the main body of the paper, the blue points are cloud-size measurements, while the yellow points are within the FWHM of the emission peak. The points highlighted with solid black circle are those in common between H09 and our sample. The dashed lines show L81 and S87’s relationships.

This paper has been typeset from a $\text{\TeX}/\text{\LaTeX}$ file prepared by the author.